3D Printed Surface Applicators for High Dose Rate Brachytherapy

by

Scott Alan Clarke

Submitted in partial fulfillment of the requirements
for the degree of Master of Science

at

Dalhousie University
Halifax, Nova Scotia
August 2016

Dedicated to my friends and family. Without them this work would not have been possible.

TABLE OF CONTENTS

LIST OF TABLES

LIST OF FIGURES

ABSTRACT

HDR surface mould brachytherapy is a technique used to treat various types of skin lesions including basal and squamous cell carcinoma. This work investigates the feasibility of using 3D printed surface applicators for the treatment of HDR brachytherapy. An extensive phantom study was conducted to assess various treatment locations on the body, including the ankle and the nose. 3D printed applicators were digitally designed and customized using the existing patient CT set. Radiation plans were generated for two applicator types: Freiburg Flap and 3D printed. Within the plan, critical target volumes (CTVs) and organs-at-risk (OARs) were contoured to analyze the quality of the plan created by the two applicator modalities by studying their respective dosimetric properties obtained from a dose-volume histogram (DVH). Due to the inverse square properties of the source, we also were concerned with the air gaps between the applicator and the skin. We found that the radiation plans for the 3D printed applicator yielded comparable or better dose distributions compared to Freiburg Flap applicators, with notable improvements on the nose study. The volume of air gaps between applicator and skin also dropped 98% and 58% for the ankle and nose study, respectively. These findings have allowed us to begin using 3D printed applicators for patients within the clinic receiving HDR brachytherapy for treatment of the skin.

LIST OF ABBREVIATIONS USED

UV	Ultraviolet
DNA	Deoxyribonucleic Acid
BCC	Basal Cell Carcinoma
SCC	Squamous Cell Carcinoma
HVL	Half-Value Layer
LDR	Low-Dose Rate
HDR	High-Dose Rate
Ir-192	Iridium-192
I-125	Iodine-125
Pd-103	Palladium-103
Te-125	Telluruim-125
SSD	Source to Surface Distance
OAR	Organ at Risk
GTV	Gross Tumour Volume
CTV	Clinical Target Volume
ITV	Internal Target Volume
PTV	Planning Target Volume
MRI	Magnetic Resonance Imaging
CT	Computed Tomography
DVH	Dose-Volume Histogram
EBRT	External Beam Radiation Therapy
IPSA	Inverse Planning Simulated Annealing

FF	Freiburg Flap
DHI	Dose Homogeneity Index
MERT	Modulated Electron Radiation Therapy

ACKNOWLEDGEMENTS

I would like to begin by offering my sincere thanks to my supervisor, Dr. Mammo Yewondwossen, for his help completing this project over the course of this past year. From classroom to the lab, your vast amount of knowledge has rubbed off on me more than you know. Thank you for always being there to answer my many questions, whether related to this project or just about medical physics in general. The research environment which you created has made being your student a pleasure.

I would also like to extend my thanks to Dr. James Robar for everything he has done for me. From making the trip to Mount Allison University to inspire a soon-to-be graduate without a plan to take the step to become a Dalhousie Tiger, to the many opportunities that have come from that. Thank you to Dr. Krista Chytyk-Praznik for always being there to answer my endless stream of questions and always being available for help.

Additionally, thank you to everyone within the Nova Scotia Cancer Centre for sharing a great deal of knowledge with me over the past two years. A special thanks goes to Jim Allen for always being a phone call away when the 3D printers act up.

I would also like to thank my fellow lab mates: Dave Parsons, Lee MacDonald, Dr. Tynan Stevens, and Wesley Bowman. There was never a dull moment working with you. Wesley, without your Blender and coding assistance this would not have been possible.

Finally, I would like to thank my friends and family for their support over the past two years. Most importantly, thank you Hannah.

CHAPTER 1 INTRODUCTION

1.1 Skin Cancer

The skin is the largest organ in the human body. It serves as the barrier separating the internal organs of an organism from the exterior world, making it a very important part of the immune system. It serves homeostatic functions and helps the body generate vitamin D through a series of chemical reactions driven by ultraviolet light (1,2). The skin behaves as the first line of defence against bacteria, viruses, and ultraviolet rays from the sun, among other things. This harmful radiation can penetrate the cellular and nuclear membranes of skin cells and interact with DNA potentially causing mutations. When normal cells detect an error in a DNA strand, they undergo a series of reactions that ultimately lead to the destruction of the cell. Cancerous cells have the ability to bypass these regulation mechanisms, by activated repair protiens and tumour suppressor genes, to allow growth to continue. As the mutated DNA copies itself, it further spreads the mutation, causing out of control growth and can lead to cancer.

Skin cancer is the most common type of cancer, affecting nearly 3 million people worldwide each year. This number is expected to grow as the ozone layer is depleted, removing the natural filtering method of UV rays. It is estimated that a 10% decrease in ozone levels will result in the incidence of skin cancer rising by about 300,000 cases (3). The main factors that contribute to developing skin cancer include a history of sun burns, a fair complexion, and prolonged exposure to the sun (2,3). There has been an upward trend in the number of documented skin cancer cases over the past 30 years. However, analyzing the data from the most recent five years indicates that the trend is slowing down and beginning to plateau for those under the age of 50 (4).

There are many layers that compose the skin. Superficially, the epidermis is composed of four to five layers (depending on the region of the body): the stratum corneum, stratum lucidum, stratum granulosum, stratum spinosum, and stratum basale (5). Different types of skin cancers affect different layers of the skin. The three main types of cancer associated with the skin are squamous cell carcinoma (SCC), basal cell carcinoma (BCC), and melanoma.

1.1.1 Squamous Cell Carcinoma

Affecting about 20% of all skin cancer patients, SCC is a type of cancer that is generated in the more superficial layers of the skin (2). SCC is highly treatable and not usually considered to be life-threatening, but if left untreated it can spread to nearby regions causing serious complications (6). These cancers are known to appear on areas of the body that are usually exposed to the rays of the sun, such as the nose, ears, lips, and hands (2).

1.1.2 Basal Cell Carcinoma

Accounting for about 75-80% of diagnoses, BCC is the most common type of skin cancer (3). It gets its name due to its area of origin - the basal cells located within the stratum basale. Similar to SCC, BCC generally develops in the regions of the body that receive prolonged exposure to the sun. BCC is slow growing and often not life-threatening, however, early treatment is recommended to stop the spread to the bones and surrounding tissue.

1.1.3 Melanoma

Although melanoma is the least common type of skin cancer, it results in the most deaths. This type of cancer is caused from the mutation of melanocytes that are located in the lower regions of the epidermis. Melanocytes are a type of cell in charge of producing melanin, the pigment that is responsible for giving skin its natural colour. It is estimated that over 76,000 new cases of melanoma will be discovered in 2016 resulting in over 10,000 deaths in the United States (7). As is the case with SCC and BCC, people who overexpose themselves to natural or artificial UV rays are at a greater risk of developing melanoma at some point in their lifetime.

1.2 Treatment

When SCC is detected early it can be treated with surgical extraction. However, if it is left untreated, SCC can penetrate into the deeper layers of the tissue and metastasize to other areas of the body. There are several different treatment options to follow depending on the tumour size, type, location and depth (8). The typical treatment options include surgery, radiation, chemotherapy, or a combination of the three. The goal of treating cancer is to assess two factors: 1) The five-year survival rate and 2) the burden to the patient. The five-year survival rate is the probability that a patient will still be alive in five years, with or without a recurrence of the disease. If the disease has not recurred in that time, there is a high probability it will not come back at all. The second factor, the cost to the patient, is a measure of quality of life. For skin cancer patients, this is usually a cosmetic concern. The benefits of treating the tumour need to outweigh the harm that it may do to the body.

1.3 Treatment with Radiation

Among all patients diagnosed with cancer, about 50% will receive radiation therapy either before, during, or after surgery (9). Radiation therapy uses ionizing radiation to penetrate the cell membrane of cancerous cells and interact with the DNA, causing damage. Cells respond differently to radiation depending on which stage of the cell cycle it is in. Cell death mostly occurs during the S phase, where DNA is condensed and replicated. Because all cells within a tumour are not in the same phase of the cell cycle, a fractionated radiation plan can allow some cells to continue through their cycle until they reach a phase that will respond more effectively to radiation.

Ionizing radiation can come in many forms, ranging from particulate matter like electrons, protons, or α-particles, to uncharged particles, such as x-rays or γ-rays. Depending on the incident particle, radiation can be either classified as directly ionizing or indirectly ionizing. Charged particles fall into the category of directly ionizing radiation, meaning the individual particles have enough kinetic energy to disrupt the atomic structure of the absorbing medium causing chemical and biological changes (10). Electromagnetic radiation such as x-rays and γ-rays are considered indirectly ionizing. This is because their photons do not cause chemical or biological damage to cells directly but they transfer their energy to fast moving charged particles which are able to produce cellular damage. The deposition of energy from indirectly ionizing radiation is sometimes referred to as a two-step process. The first step is the photon interaction, described in Sections 1.3.1 and 1.3.2, which produces secondary charged particles. The second step is the interaction of those charged particles within the cell of an organism producing damage leading to cell death.

X-rays and γ-rays differ only in their production. X-rays are generated through extranuclear interactions while γ-rays are generated intranuclearly (10). The energy of a photon, *E*, is proportional to its frequency and inversely proportional to its wavelength:

$$E = h\nu = \frac{hc}{\lambda} \quad (1)$$

where h is Planck's constant, ν is the frequency of the photon, c is the speed of light, and λ is the wavelength of the photon.

X-ray photons are generated when an excited electron drops an energy level within an atom (called characteristic x-rays) or when a particle is decelerated in an electric field (bremsstrahlung x-rays). X-ray photons can be organized based on their energy as follows (11):

Table 1 - Different classes of x-ray photons based on energy.

Energy Range	Classification
0.1 - 20 keV	Low-energy (soft) x-rays
20 - 120 keV	Diagnostic x-rays
120 - 300 keV	Orthovoltage x-rays
300 keV - 1 MeV	Intermediate-energy x-rays
1 MeV +	Megavoltage x-rays

There are various processes by which photons can interact. The probability of an interaction (and the type of interaction) occuring depends on their energy as well as the chemical composition of the absorbing material, specifically, the atomic number (Z). The photoelectric effect is the dominant process for low energy photons striking a high atomic

number target, the Compton effect dominates at intermediate photon energies, and pair production at high energies (11).

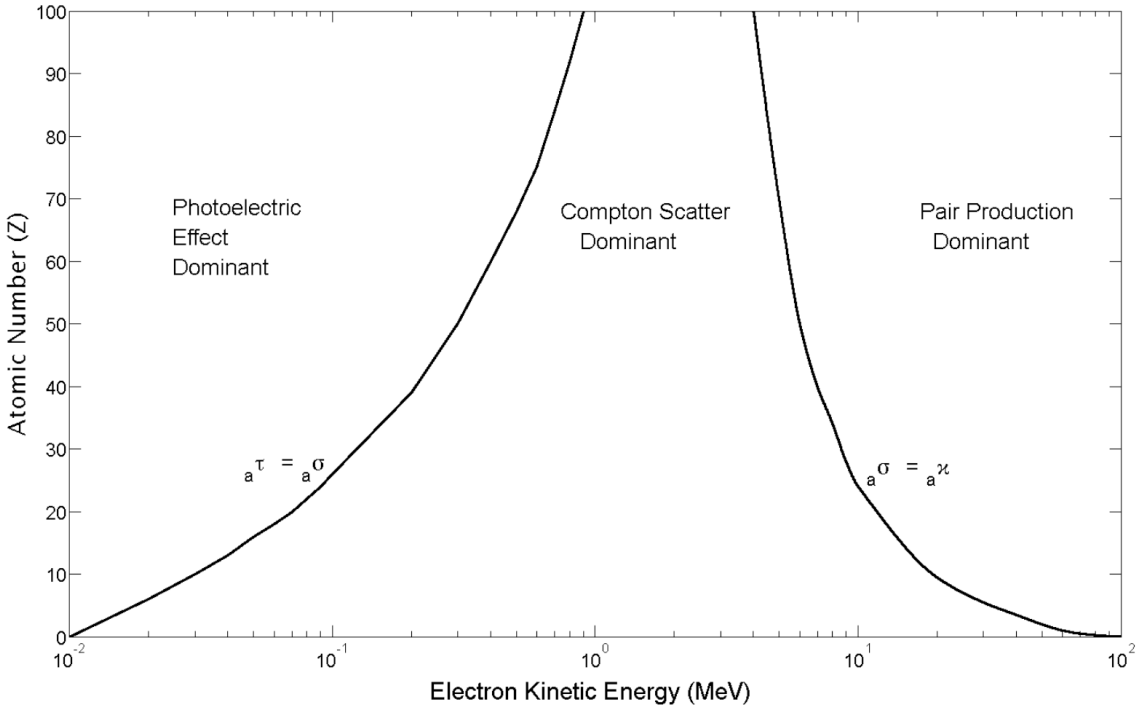

Figure 1 - Relative importance of major types of photon interactions (11).

1.3.1 The Photoelectric Effect

The photoelectric effect occurs when an incoming photon interacts with a tightly bound, inner-shell electron. The electron typically comes from the K, L, or M shell of an atom in the absorbing material. All of the photon energy is absorbed by the electron, with some energy used to overcome the binding energy of the electron. The remainder is transferred to the electron as kinetic energy, KE_{e^-} (10),

$$KE_{e^-} = h\nu - E_B \tag{2}$$

where E_B is the binding energy of the electron and $h\nu$ is the incident photon energy. If the energy of the incoming photon is not greater than the binding energy holding the electron to the atom, no interaction will take place. The vacancy left from the

ejected electron results in a characteristic x-ray being emitted of about 0.5 keV, which has little biological effect (10).

1.3.2 The Compton Effect

The state of the target electron is what defines the difference between the Compton effect and the photoelectric effect. In the photoelectric effect, the electron was bound to the nucleus. In Compton scattering (shown schematically in Figure 2), the target is a "free" electron, where the binding energy is approximately zero compared to the incoming photon energy (11). The incident photon gets absorbed and transfers a portion of its energy to the electron, while the photon is scattered through an angle, θ, and continues on a new trajectory. The Compton process is dominant at the intermediate energy ranges for all Z values but has a larger probability corresponding to atoms with lower atomic numbers as can be seen in Figure 1. After the initial collision, there is a fast electron and a photon with slightly less energy than it had before the collision, which can continue to interact with other atoms. The production of high energy electrons from Compton scattering can result in ionization of other atoms in the absorbing material, breaking of chemical bonds, and beginning the process of biological damage.

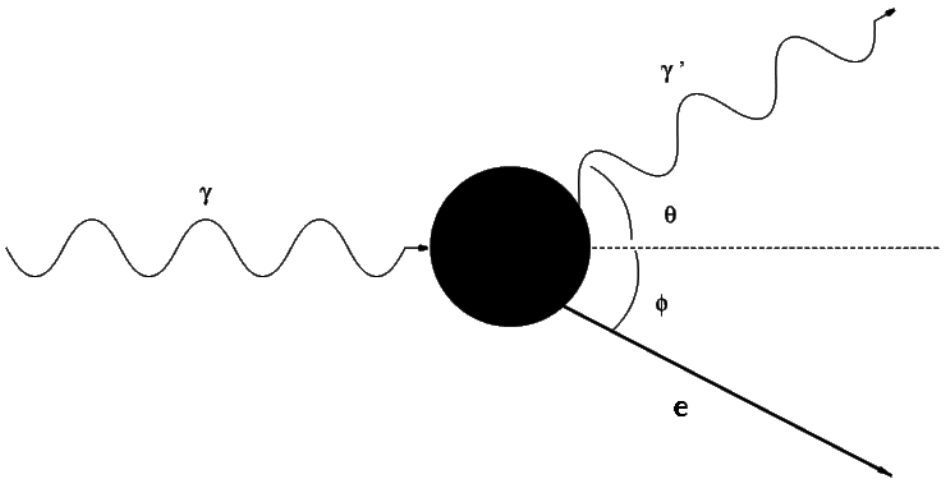

Figure 2 - Schematic of Compton Scattering. γ and γ' correspond to the incoming and redirected photon respectively while θ represents the angle of deflection of the photon and ϕ represents the angle of deflection of the electron.

1.3.3 Biological Effects of Radiation

The biological target of radiation is the genetic component of the cell – its DNA. Similar to direct and indirect ionization, there is direct and indirect action resulting from that ionization (10). Direct action of radiation is when the atoms of the medium are ionized, initiating a cascade of events that leads to biological damage. This process is dominant for particles with a high linear energy transfer (LET). LET refers to the amount of energy deposited per unit distance, with high values corresponding to larger particles like neutrons and α-particles (10). Indirect action occurs when radiation interacts with other atoms or molecules (typically water for humans) to produce highly reactive free radicals which are able to do damage to critical structures. A flow chart of how indirectly ionizing radiation interacts with the body is shown in Figure 3. Free radicals are created when an atom or molecule has an unpaired electron in its outer most shell. In the cell, the radical form of water reacts with another water molecule to produce the highly reactive

hydroxyl radical ($OH\cdot$), which is estimated to produce about two-thirds of x-ray damage to DNA (10):

$$H_20^+ + H_20 \rightarrow H_30^+ + OH\cdot \tag{3}$$

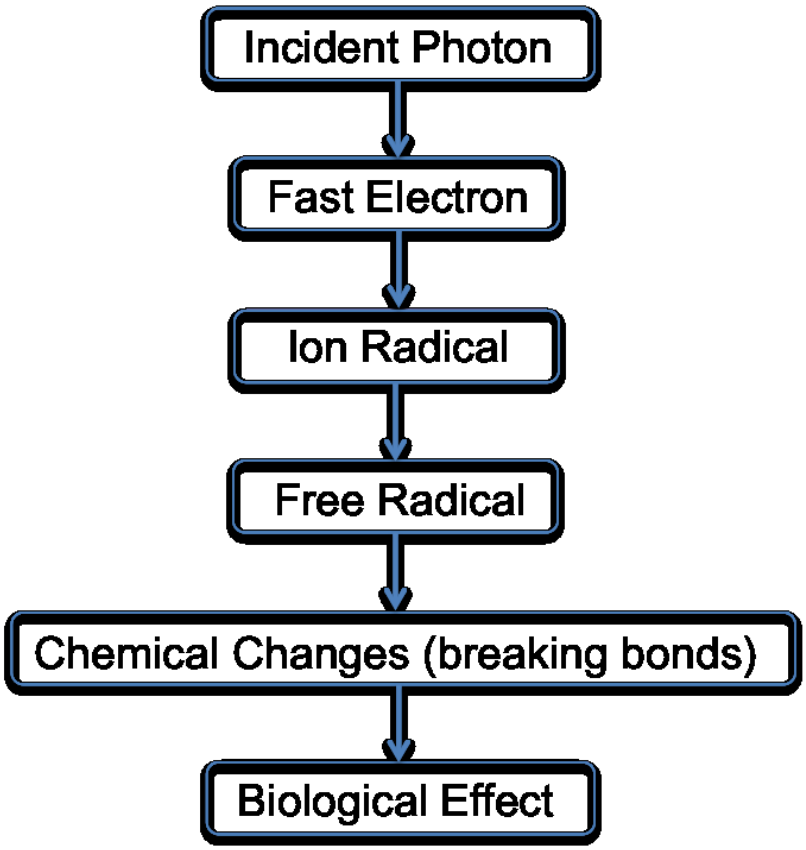

Figure 3 - Flow of indirect action of radiation. Adapted from Hall (10).

DNA is a large molecule that makes up the genetic information of every cell in the body. It has a characteristic double helix shape, resembling a twisted ladder, held together by hydrogen bonding of certain base pairs. All DNA is coded by different combinations of the same four base pairs: adenine, guanine, cytosine, and thymine. Within a molecule of DNA, cytosine can only form bonds with guanine, and adenine can

only form bonds with thymine. This results in the two strands that make up DNA being antiparallel and complementary to one another.

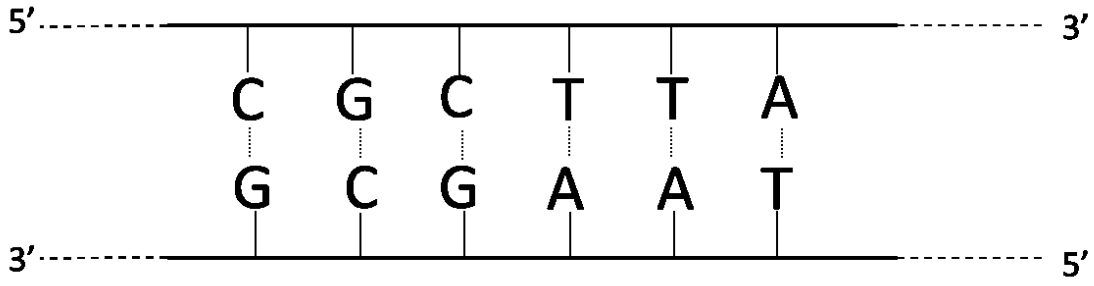

Figure 4 - Schematic illustration of DNA double helix showing complementary, antiparallel strands.

Damage to DNA can occur in various forms, ranging from a single base pair mutation to a breakage in the sugar-phosphate backbone. Base pair mutations are typically easily fixed and do not result in death to the cell. The body has generated mechanisms to repair single base pair damage by removing the damaged base and replacing it with a functional one, allowing the DNA to continue its function. If radiation is absorbed within the DNA, a break in one of the two backbone strands could occur resulting in a single strand break (SSB). SSBs are often repaired by the cell using the complementary strand as a template.

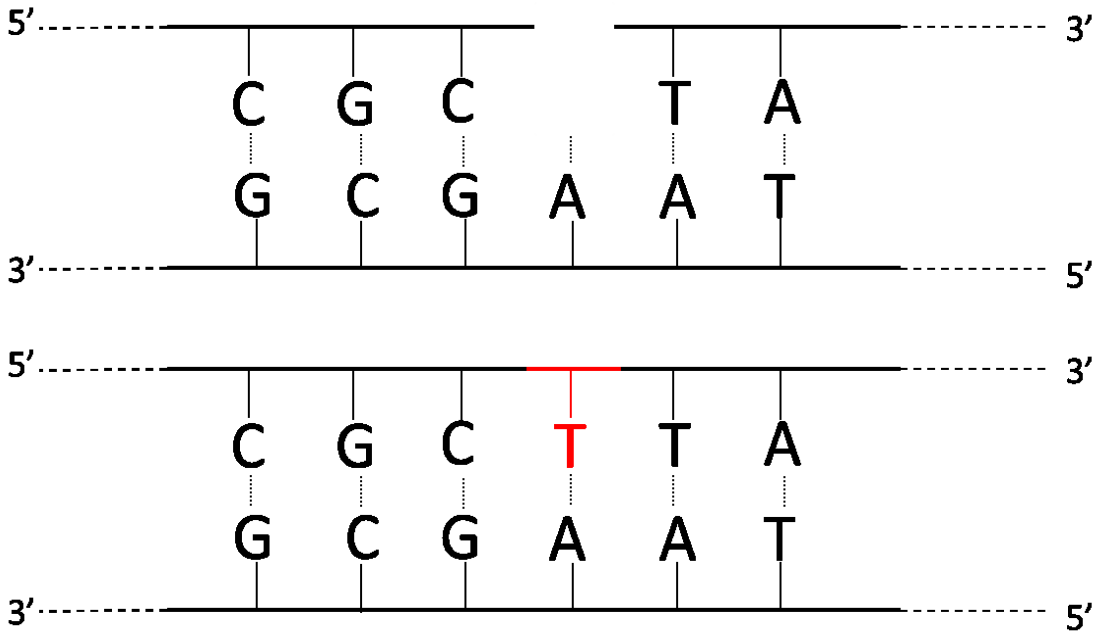

Figure 5 - Top: SSB on top strand of DNA molecule. Bottom: Repair using complementary strand.

A double strand break (DSB) occurs when damage is done to the backbone on both strands of the DNA molecule. The result is cleavage of DNA into two pieces, rendering it ineffective and halting the cell's life cycle. DSBs are believed to be the integral component involved in cell death by radiation (10). If the two strands are broken far apart from one another, the cell undertakes similar repair protocols as in SSBs. The incidence of DSBs is estimated to be approximately 0.04 times the incidence of SSBs, with the number of DSBs increasing linearly with increasing dose. This indicates they originate from a single track of ionizing radiation (10). Both direct and indirect ionizations can result is a double strand break depending on the incident energy. If the particles are large (neutrons, α-particles, etc), they could damage many base pairs at once, increasing the likelihood that cell death will occur.

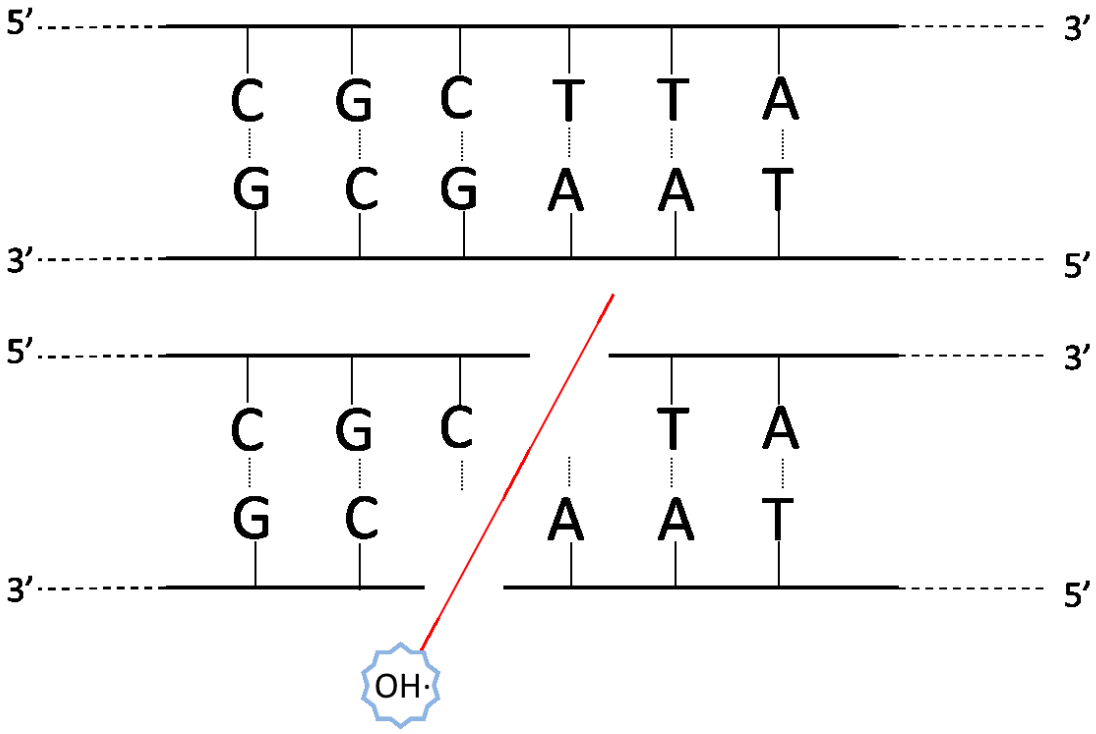

Figure 6 - Top: Normal strand of DNA. Bottom: DSB caused by the hydroxyl radical, separating the molecule into two pieces.

1.4 Radiation Techniques of Skin Cancer Treatment

Radiation treatment of skin cancer can be administered in a variety of different ways. The common factor in each technique is that the radiation must be delivered superficially, sparing as much of the underlying tissue as possible. For this reason, most skin cancer patients that are eligible for radiation treatment receive either electron therapy, orthovoltage therapy, or brachytherapy.

1.4.1 Electron Therapy

Electron therapy is most useful in the energy range of 6 to 20 MeV, allowing for treatment of superficial lesions that are less than 5 cm deep (12). Electrons travel through the tissue and interact with atoms or other electrons via a Coulomb field. The four main

processes by which these interactions occur are inelastic collisions with atomic electrons, inelastic collisions with nuclei, elastic collisions with atomic electrons, and elastic collisions with nuclei (12). In low atomic number media, such as human tissue, electrons primarily lose their energy through ionizing events with atomic electrons. As a beam of electrons travels through a patient, their energies are continually diminished until they reach thermal energies and the electron can be captured by surrounding atoms within the tissue.

Electrons deposit their energy to the patient as absorbed dose. The dose is defined as the energy absorbed per unit mass of tissue and can be calculated knowing the electron fluence and collision stopping power. The fluence (Φ) is defined as the number of particles per unit area and the collision stopping power is defined as the rate of energy loss resulting from the sum of the soft and hard collisions (11).

Soft collisions occur when an incident electron passes by an atom at a distance much larger than the radius of the atom. Such an interaction causes the excitation of an outer shell electron to elevate to a higher energy level, or escape the pull of the atom altogether. The amount of energy necessary to excite the bound electron is determined by the binding energy, resulting in a small amount of energy being transmitted from incident electron to the absorbing medium. Since the incident electron does not come in contact directly with the atoms of the absorbing medium (considering the amount of empty space in an atom), soft collisions are much more frequent than hard collisions.

Hard collisions occur when the incident electron interacts with an atom of the absorbing material on the order of the radius of the atom. The incident electron collides

and ejects an orbital electron, which can cause further ionizations called delta rays (δ-rays).

The collision stopping power, $\left(\frac{S}{\rho}\right)_{col}$, is defined as the ratio of energy lost by a charged particle (dE) to the distance travelled as a result of the collisions (dl), which can then be used to calculate the absorbed dose, D (12):

$$\left(\frac{S}{\rho}\right)_{col} = \left(\frac{dE}{\rho dl}\right)_{col} \tag{4}$$

$$D = \int \Phi_E \cdot \left(\frac{S}{\rho}\right)_{col} dE \tag{5}$$

The electron beam energy is typically chosen such that the entire treatment volume lies within the 80-90% isodose line, provided there are no critical structures beneath the tumour. The 100% isodose line is defined as the area of the tissue receiving 100% of the prescribed dose. Beyond the 80% depth dose, the dose fall off is characteristically rapid (12). A typical two-dimensional isodose distribution is shown in Figure 7, illustrating the lateral constriction at higher isodose values and the broadening of low isodose levels caused by increased scatter.

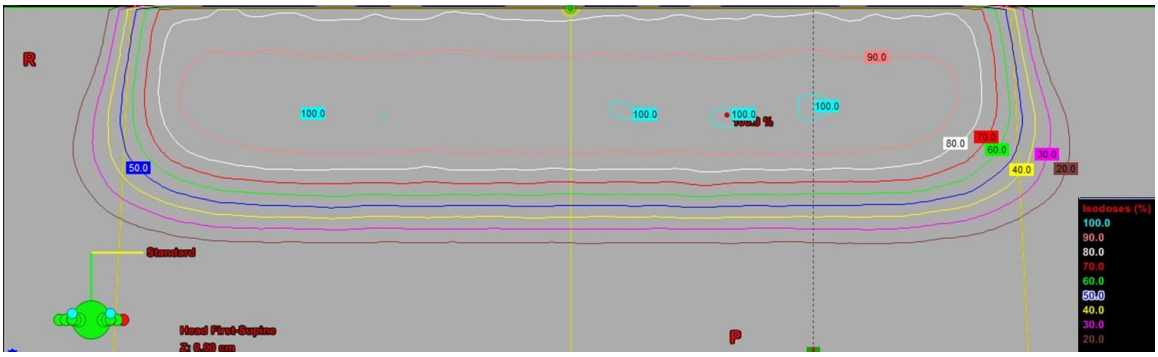

Figure 7 - 2D electron dose distribution showing bulging of lower isodose lines (13).

The unique dose deposition of electrons causes them to have many advantages for treating superficial lesions. Referring to Figure 9, the characteristic sharp fall off of electrons can be seen compared to 300 keV orthovoltage photons. The bremsstrahlung tail is due to the generation of photons from inelastic collisions of the beam with atomic nuclei of the tissue. This also allows for increased dose homogeneity within the treatment volume resulting in an increase in tumour control. Despite the many advantages of treating with electrons, there are also some disadvantages, primarily when it comes to irregular surfaces. Due to the negative charge of electrons, they scatter at a much higher rate than other treatment beams, such as photons. This results in more unwanted periphery dose to the surrounding tissue.

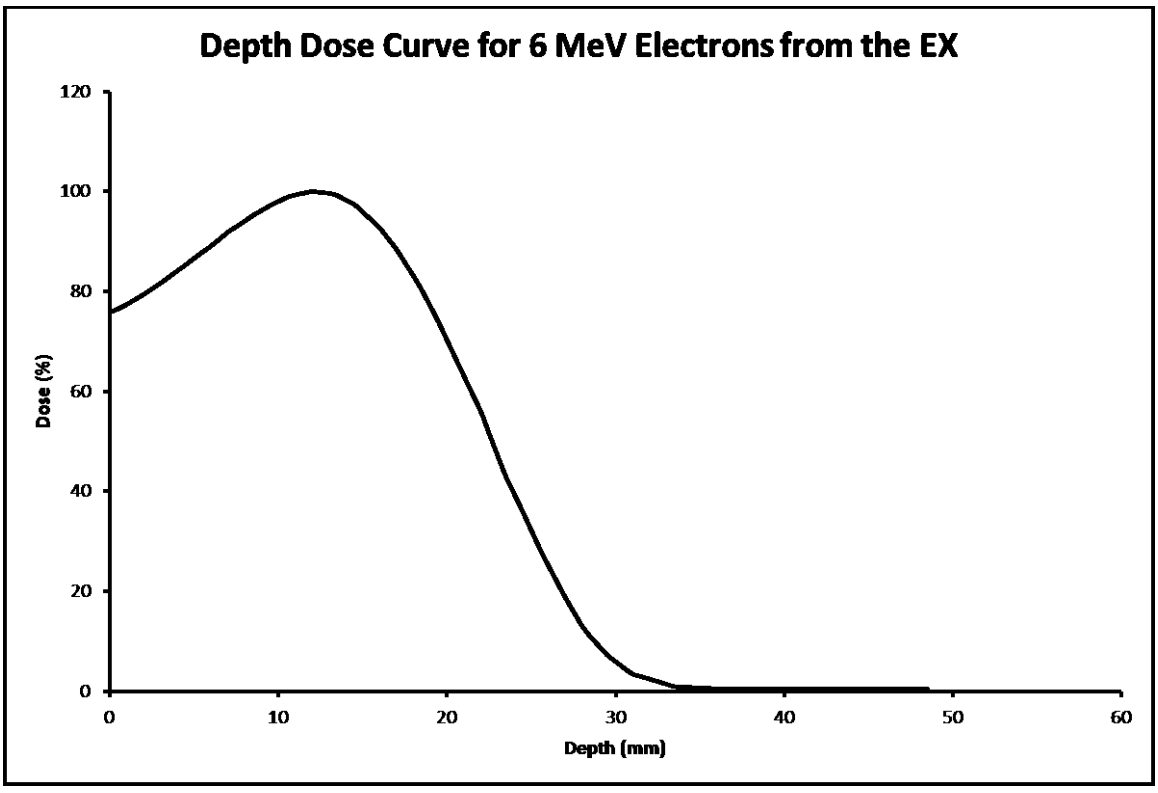

Figure 8 - Depth dose curve of an electron beam taken from the 2100EX linac at the Nova Scotia Cancer Centre.

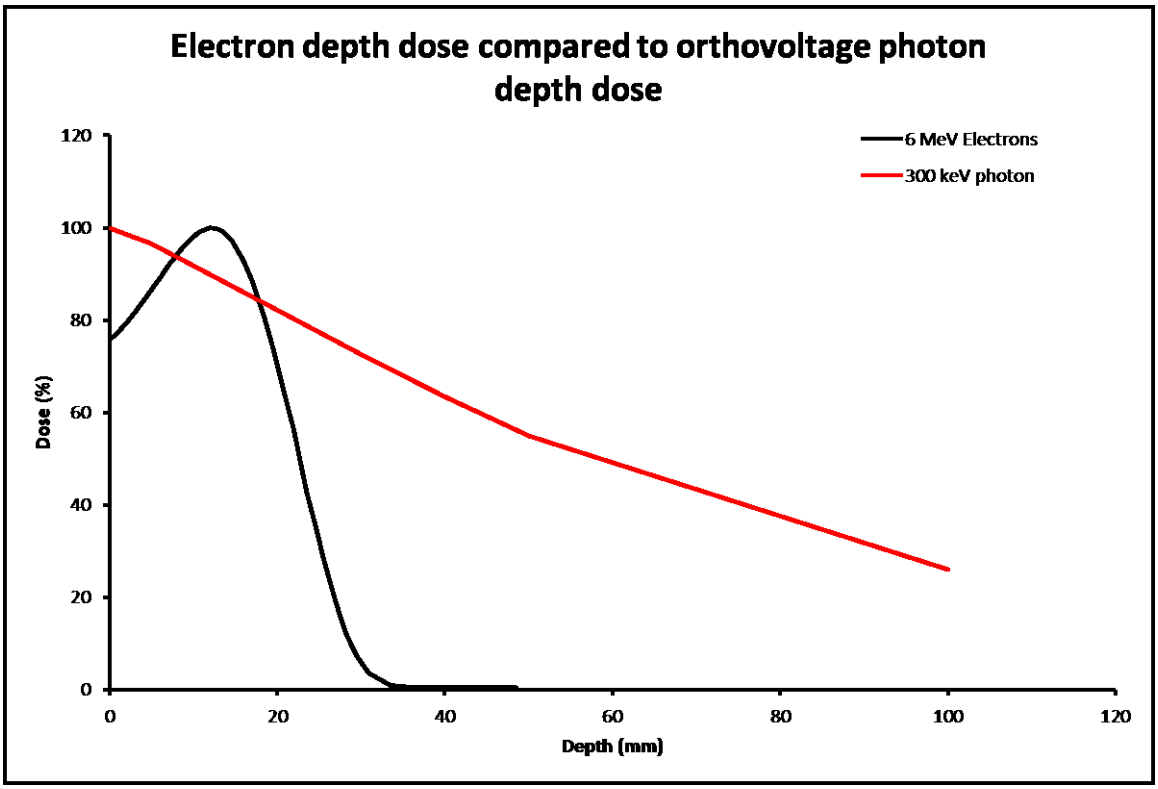

Figure 9 - Black: Electron depth dose curve. Red: Orthovoltage photon depth dose curve.

1.4.2 Orthovoltage X-ray Therapy

Superficial, or orthovoltage, therapy refers to x-rays produced in the energy range of 50 to 300 kV (12). The x-rays are generated via an x-ray tube, which requires three basic elements in order to function: a source of electrons, a potential difference to accelerate these electrons, and a target to decelerate them, producing bremsstrahlung photons. The efficiency of x-ray production is on the order of 1%, with the remaining electron energy being lost as heat deposited in the target (12). The low energy, or soft, x-rays can be filtered out using layers of absorbing material, such as aluminum, resulting in a uniform energy beam. The amount of filter material depends on the half-value layer (HVL), defined as the thickness of material to reduce the exposure rate by one half its original value. HVL is a function of the attenuation coefficient, μ, and is defined as:

$$HVL = \frac{\ln(2)}{\mu} \tag{6}$$

The typical HVL values used in the superficial energy range are 1-8 mm of Aluminum or 1-4 mm of Copper (12). The maximum dose occurs close to the surface of the skin, with 90% of the max value occurring within a 2 cm depth. A disadvantage of using orthovoltage photon therapy is the dose to bone. The energy of a typical orthovoltage photon (200-300 kV) lies within the photoelectric region of the photon interaction curve (see Figure 1). Bone, having a higher atomic number than the surrounding tissue, absorbs more dose in this region due to the Z^3 dependence of the photoelectric effect. If irradiating bone cannot be spared, an alternative treatment method is used.

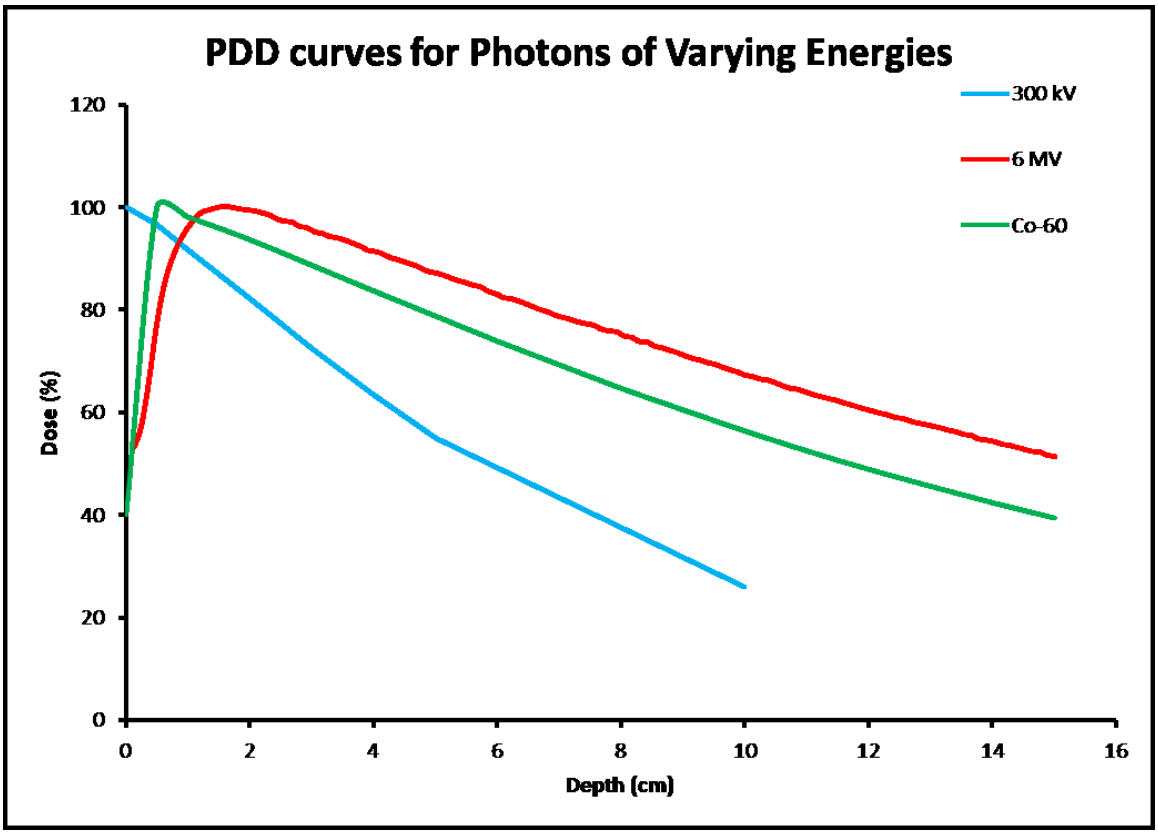

Figure 10 - Depth dose curves in water for various beam energies. 6 MV photons (red), 300 kV orthovoltage photons (blue), and Co-60 (green).

Orthovoltage therapy for treating skin cancers of the face have been proven to yield more cosmetically desirable results for patients when compared with surgical excision (14).

1.5 Brachytherapy

Seven years after the discovery of radioactivity, Alexander Graham Bell first suggested the idea of what has become brachytherapy by saying "…there is no reason why a tiny fragment of radium sealed in a fine glass tube should not be directly inserted into the very heart of the cancer, thus acting directly upon the diseased material…" (15). The general concept of brachytherapy has remained the same: introduce a sealed radioactive source (seed) into close proximity of a diseased area and allow the natural decay of the source to irradiate the tissue. Modern brachytherapy is much more sophisticated than it was in the past, typically being used to treat gynecological, prostate, and skin cancers. Brachytherapy has been used clinically as a primary treatment modality, along with surgery, or as a boost given in addition to external beam radiation. Radium sources have been replaced with radioactive isotopes offering a wider range of energies and activities used to treat many different locations around the body.

The two main types of brachytherapy, low dose rate (LDR) and high dose rate (HDR), differ primarily in the activity of the source. The activity is defined as the product of the number of nuclei of the source, N, and the decay constant of the material, λ. Mathematically, it can be represented as:

$$-\frac{dN}{dt} = \lambda N \tag{7}$$

The decay constant is measured in units of reciprocal time and inversely related to the half-life, $\tau_{1/2}$, of the material, the amount of time that needs to pass in order for half of the original material to decay.

$$\tau_{1/2} = \frac{\ln(2)}{\lambda} \tag{8}$$

1.5.1 Low-Dose Rate Brachytherapy

LDR sources, characteristic of their low activities, are generally left in the patient permanently. These sources are classified as having an activity that does not exceed 2 Gy/hour. The most common sources for LDR are Iodine-125 (I-125) and Palladium-103 (Pd-103) (16). I-125 decays exclusively by electron capture to an excited state of Tellurium-125 (Te-125), which then decays to its ground state while emitting a 35.5 keV photon. This decay scheme also emits characteristic x-rays ranging from 27 to 35 keV. Seeds made of palladium decay in a similar manner to iodine seeds, with x-rays in the range of 20-23 keV (12). LDR brachytherapy is most commonly used in treating prostate cancer, where anywhere from 60 to 100 seeds, each about the size of a grain of rice, will be inserted through the perineum via ultrasound guidance. Once the seeds have been implanted, the patient is able to leave while the radiation is being delivered. The energy of the x-rays emitted from the seeds is low enough such that they do not pose any harm to the general public. The prescribed dose will be delivered to the organ over a period of weeks to months, after which no measureable radiation will emit from the seed allowing them to stay in the patient permanently.

1.5.2 High-Dose Rate Brachytherapy

The development of remote afterloaders (Figure 11) made it possible for physicians to be outside of the room while treatment was being delivered, allowing for higher activity sources to be used. This is what is now known as HDR brachytherapy. HDR brachytherapy uses sources with activities greater than 12 Gy/hour to treat patients. Iridium-192 (Ir-192) decays with an average energy of 380 keV and a half-live of 73.8 days (12). The seeds are cylindrical, measuring 3 mm long and 0.5 mm in diameter (17).

The afterloader is a sophisticated piece of equipment that determines where the source will go, the amount of time it will stay there, and it provides shielding when not in use. Before the source is sent out to its destination, a check cable fitted with a dummy source of similar dimensions to the actual source is sent out to ensure that there are no obstructions in the catheter and that the treatment can proceed without interruption. An obstruction in a catheter could result in the source getting stuck, creating an emergency that could overdose the patient and expose staff. Once the check cable has been fed through every catheter being used, the treatment can begin. Following precisely the same path as the dummy source, the computer-guided radioactive source is fed from the afterloader to the predetermined “dwell” positions, for a calculated amount of “dwell” time, to deliver dose to the patient. Once the treatment is completed, the source is retracted into the afterloader to shield staff and others in the room.

Figure 11 - MicroSelectron remote afterloader, made by Elekta. Photo taken from the Nova Scotia Cancer Centre.

Table 2 - Common radioactive isotopes and their properties. Adapted from Devlin (18).

Isotope	Emission Type	Half-life (days)	Energy (keV)
^{198}Au	γ	2.7	412
^{131}Cs	γ	9.7	34
^{137}Cs	γ	30 years	662
^{125}I	x-ray	59	27-35
^{192}Ir	γ	74	380
^{103}Pd	x-ray	17	20-23
^{60}Co	γ	5.26 years	1.17, 1.33 MeV

1.5.3 Brachytherapy Treatment of the skin

One of the primary benefits of using brachytherapy over external beam therapy (such as MV photons, orthovoltage photons, or electrons) is the dosimetric characteristics of the radioactive source. Governed primarily by the inverse square law, the source is able to administer the bulk of its dose in close proximity while sparing the surrounding tissue. This property can also have negative side effects, resulting in a large amount of dose in tissues near the source, which can be detrimental to the patient. If the source is held too close to the skin for an extended period of time, non-healing ulcerations can develop, requiring immediate medical attention (19). Applicators have been developed to place the source at a desired distance away from the skin, ensuring that the hot spots are localized within the applicator and not the patient. HDR brachytherapy used in combination with surface moulds or applicators have been proven to be an effective method of treatment for superficial lesions extending a few millimetres below the surface of the skin. BCC and SCC are often successfully treated with this technique resulting in excellent tumour control and few cosmetic defects (20).

Common HDR brachytherapy skin applicators include the Leipzig and Freiburg Flap (FF), or wax moulds. A Leipzig applicator, shown in Figure 12, is primarily used for smaller lesions (diameters less than 25 mm) that are not irregular in shape. The applicators are made of a tungsten/steel alloy and consist of a cone-shaped collimator and a plastic cap to absorb scattered electrons (21). The iridium source is fed into the applicator via a catheter, guided by the afterloader, and sits at the apex of the cone to deliver radiation downward towards the skin. The dose distribution can be altered depending on whether the source is parallel or perpendicular to the treatment plane, as

well as the amount of time that the source is held in the applicator. The Source-to-surface distance (SSD) for the Leipzig applicator is a constant 1.6 cm (21). Leipzig applicators are rather limited in the size of the treatment field, as no applicators are made with a cone diameter larger than 30 mm. For larger lesions, other types of applicators are required. Valencia applicators are similar to Leipzig in shape and composition but differ in dose distribution. Valencia applicators, shown in Figure 12, have a flattening filter to allow the dose to enter the patient perpendicularly.

Figure 12 - 30 mm Leipzig applicator (Left). 30 mm Valencia applicator (Right).

Figure 13 – Top view 30 mm Valencia applicator (top) and Leipzig applicator (bottom).

For lesions larger than 30 mm in diameter, a different approach is necessary for administering HDR brachytherapy. Wax moulds can be used to fit the contours of the patient's body and allow for complete customization of the catheter distance from the treatment plane. Like Leipzig applicators, wax moulds require that the tumour be accessible and superficial, only reaching a few millimetres below the surface of the skin. The most common locations for wax moulds are proximal to the nose and ears. The moulds are made by individually heating sheets of wax and conforming them to the contours of the patient either directly on the skin or onto a thermoplastic immobilization mask. The nature of building the moulds one layer at a time allows the therapist to have increased control over the distance from the source to treatment location, the orientation

of the catheters, and the possible dwell positions for the source. Typical catheter depths are anywhere from 3-5 mm depending on the depth of treatment required and the size of the tumour. It is important that the mould covers the entirety of the tumour to ensure that sufficient dose is being delivered to treat the disease. Margins of about 2 cm are added in all directions around the lesion to ensure that the mould is large enough and that the source can provide adequate radiation for full treatment coverage. The process of wax mould fabrication is laborious and time-consuming. If the fabricated mould does not generate the desired dose distribution, it is rendered unusable and the process begins anew. In order to generate a mould that can be used clinically, sometimes multiple iterations are required to fabricate a suitable mould, resulting in a delay in the beginning of treatment.

Similar to the moulds made out of wax, a Freiburg Flap applicator is used for treatment sites that are too large for Leipzig applicators. They also generally require a thermoplastic immobilization mask to provide a secure foundation to maintain their shape. The flaps are made of sheets consisting of silicone spheres 1 cm in diameter. Catheters are inserted into predrilled tunnels within the spheres to allow the source to move freely to the dwell positions at an SSD of 5 mm. The sheets are flexible and can be either deformed or cut to fit the contours of the patient. Although the flaps are less labour intensive than wax moulds, they still require a great deal of fabrication time from making the mask to sewing enough of the flap material to ensure complete coverage. The sheets work best for regions of the body that do not exhibit much curvature, such as the scalp or ankle.

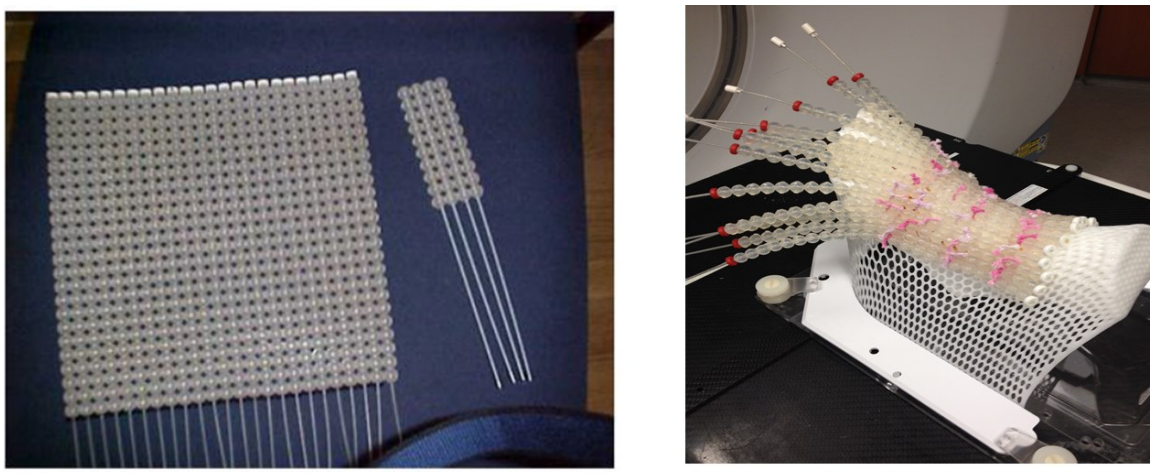

Figure 14 - Left: Sheet of Freiburg Flap fitted with catheters. Right: Freiburg Flap sewn onto thermoplastic mesh for a foot phantom.

1.6 Treatment Planning

Treatment planning is the process in which a team consisting of radiation oncologists, medical physicists, and dosimetrists create an appropriate plan to deliver radiation to the patient. The goal of this process is to deliver the prescribed dose to the diseased area, while limiting the dose to the surrounding healthy tissue. Imaging techniques, such as MRI and CT, are used to create a 3 dimensional representation of the patient to assess the various aspects of radiation therapy using a treatment planning system. Within the treatment planning system, potential organs at risk (OARs) can be contoured, as well as different target volumes to calculate the amount of dose that would be received. The critical target volumes contoured in the treatment planning system are to account for motion of the tumour during treatment as well as in between treatments, and are summarized in Table 3. Although the ITV and PTV are used to account for treatment margins, in brachytherapy the PTV does not expand the CTV and the terms are used interchangeably.

Table 3 - Definitions of various treatment volumes.

Gross Tumour Volume (GTV)	Area of malignant disease that can be seen on imaging modalities
Clinical Target Volume (CTV)	Volume extending from the GTV to account for microscopic tumour spread
Internal Target Volume (ITV)	Volume consisting of the CTV plus a margin to account for internal motion
Planning Target Volume (PTV)	Volume accounting for setup margins to ensure complete coverage of the CTV

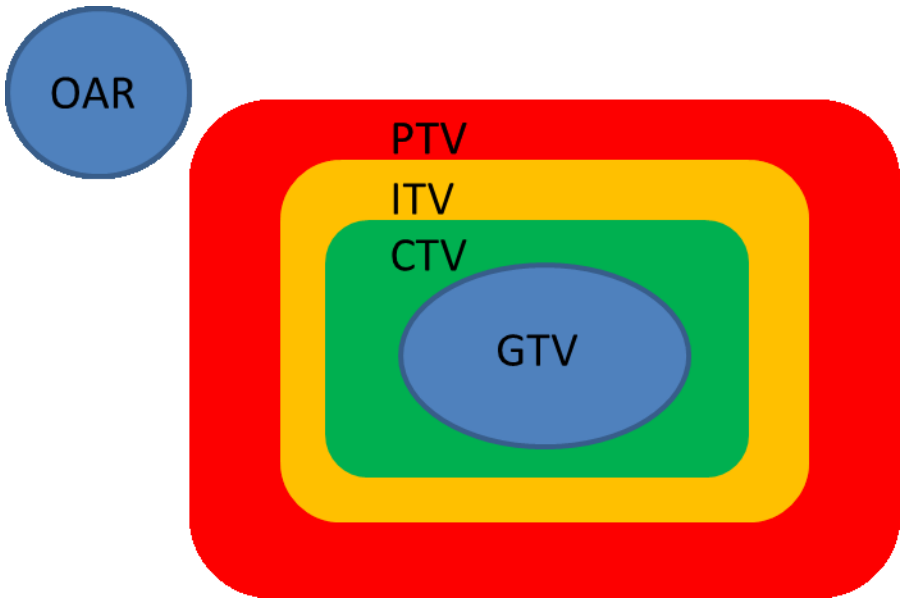

Figure 15 - Various target volumes and OAR shown graphically. Adapted from Podgorsak (23)

1.6.1 Treatment Plan Evaluation

In order for a plan to be administered to a patient, proper steps need to be taken to ensure that the dose to the tumour is sufficient to result in cell death, and the dose to the surrounding OARs is kept to a minimum. Increasing the dose to the tumour also increases

the dose to the surrounding regions. Once a plan has been created with the planning software, it must be approved by a physician who is trained to assess both the dose to the target volume and the OARs. It is often the case that multiple plans will be generated within different planning systems to ensure that the patient is receiving the best possible radiation plan. Plan evaluation is generally accomplished through analysis of dose distribution, Dose-Volume Histograms (DVH) and dose homogeneity.

The dose distribution of a given radiation plan is displayed as a series of isodose lines or colour coded washes to show regions of uniform dose, as well as high and low dose regions. DVH curves provide the quantitative information of the plan by assessing how much volume of a contoured structure is receiving a given amount of dose. The dose can be measured for any contoured structure within the patients CT image set. DVHs for the PTV and the nearby OARs are reviewed for any given radiation plan. They allow the immense amount of information contained within the planning system to be condensed into a single 2-dimensional graph that is much easier to interpret. As a result, DVHs are the most widely accepted and used tool to assess a radiation plan (12).

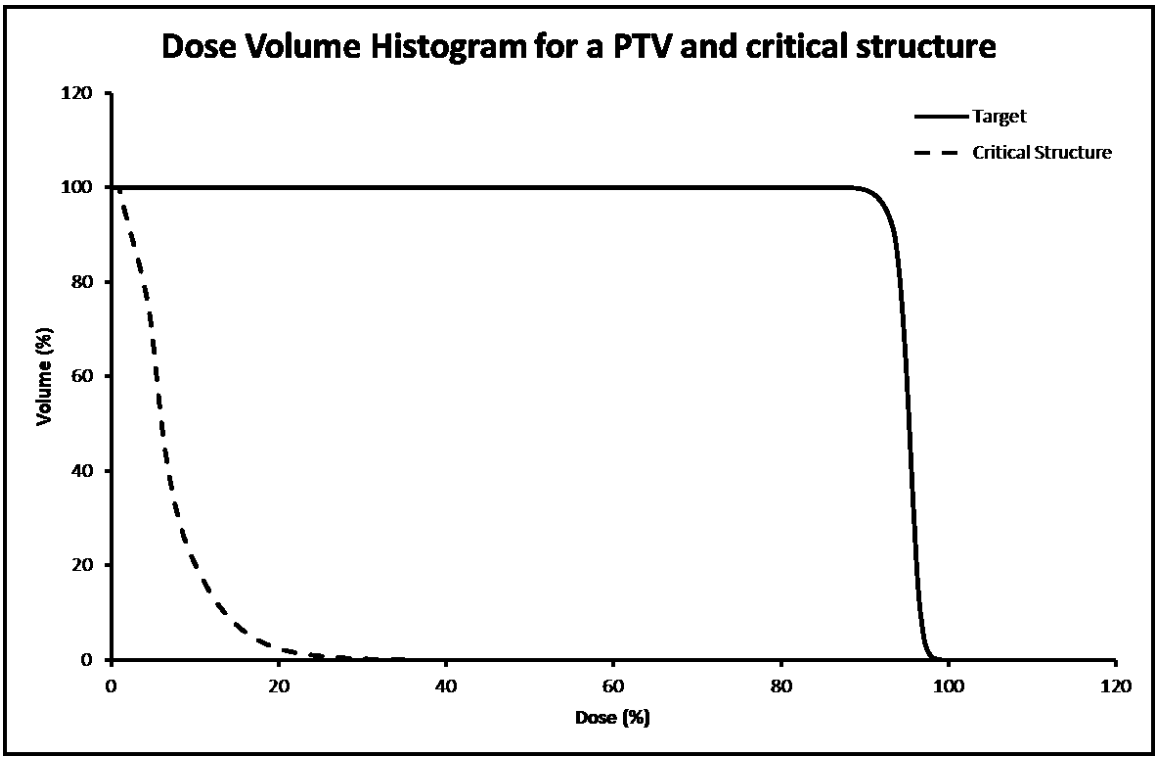

Figure 16 - Typical DVH for the target volume and an OAR. Normalized 90% dose to cover 99.5% target volume.

There are various methods to measure the quality of a radiation plan within the treatment site. Dose homogeneity index (DHI) utilizes V_{100} and V_{150} obtained from the DVH to give a value ranging from 0 to 1, where 1 indicates a more homogeneous dose delivered to the CTV (22).

$$DHI = 1 - \frac{V_{150}}{V_{100}} \tag{9}$$

The dose distribution is determined by two degrees of freedom, the dwell time and the dwell position. Unlike external beam radiation therapy (EBRT), an iridium source cannot be turned off. Reducing the dose to certain areas can be done by introducing shielding materials, increasing the SSD or decreasing the time the source remains at a given dwell position. Once the dwell positions are activated within the planning software, dwell time optimization occurs via forward optimization or inverse optimization.

Forward optimization occurs when various dosimetric parameters are initially input into the system such as maximum dose to the tumour, and an optimization algorithm aims to achieve these constraints. In inverse optimization, the dose distribution is specified using clinical objectives based on the patients anatomy before the optimization algorithm determines the parameters to obtain these objectives (20). Inverse optimization was the primary method used in this research and was accomplished with the inverse planning simulated annealing (IPSA) algorithm, where the plan is created to satisfy predetermined constraints set in place by the planner.

1.7 Applications of 3D Printing in Radiation Therapy

3D printing technology was first used by Su *et al* when developing a new technique of electron dose modulation. Modulated electron radiation therapy (MERT) involves optimizing the dose distribution with regard to dose coverage, conformity, and homogeneity within the PTV (23). MERT allows 3D printed boli to be made to fit the patient and shape the dose distribution to precisely match the contours of the PTV. Intercavitary brachytherapy applications have also been applied by a group looking to evaluate customized 3D printed gynecologic applicators. Their main purpose was to evaluate the radiation attenuation properties of PC-ISO, a type of 3D printing filament. Their results indicate that 3D printing filament is comparable to water, meaning it serves as an adequate brachytherapy applicator for patient treatment (24). It has been found that printer filament exhibits buildup characteristics within 5% of that of solid water. Surface dose can be controlled with the infill factor selected within the printer settings. 3D printed bolus also provides improved spatial conformity to the chestwall when compared to using a standard sheet bolus made of Superflab material (25).

Superficial brachytherapy applicators using 3D printers is a new technique that utilizes patient CT information to create an applicator that conforms to the curvature of the patients skin for treatment of various types of cancers. Initial work has been done by Schumacher *et al* and ongoing research is continued in this thesis (26).

1.8 Research Goals

The main goal of this research project is to develop a new HDR brachytherapy applicator for the administration of radiation to superficial lesions. With the advancement of 3D printing technology, new applicators can be fabricated to remedy the shortcomings of traditional surface applicators. Both Freiburg Flap and wax moulds require lengthy fabrication time by the practitioner. The SSD for the flaps is held at a constant 5 mm. 3D printed applicators allow for complete customization of individual catheter placement, resulting in the most ideal dose distribution for a given patient. As mentioned in Section 1.5.3, the inverse square law governs the dose characteristics of the source at the short SSD values. As a result, the SSD determines the magnitude of dose at any given point. If the source is too proximal to the surface, the dose will be too high, and too low if the source is too far away. 3D printed applicators should also improve the fit to the patient. The initial CT image set obtained from the patient's first visit is used as a template to construct the applicator to ensure that it fits precisely to the contours of their body, making this the ideal applicator for highly irregular areas such as the face and ears.

The purpose of the study is to investigate the feasibility of using 3D printers to create more conformal, reproducible, and patient specific source applicators for administering HDR brachytherapy. It is our hypothesis that implementing an in-house built algorithm for applicator customization will improve the dose distribution compared

to the status quo of treatment while greatly decreasing the need of human intervention for applicator fabrication. Once the design is created from the CT data, a 3D printer can be left unsupervised to complete the task. This lowers the fabrication time and decreases the labour intensity of the process. The objective of this thesis is achieved in two ways: through a phantom study, examining application to tumour locations of the foot and nose, and by assessing application to actual clinical cases.

CHAPTER 2 METHODS AND MATERIALS

Before any new modality of treatment can be used in a clinic, a thorough phantom study needs to be conducted to assess the accuracy of the delivered dose relative to the planned dose. In the work presented in this thesis, two areas of the body were simulated using anthropomorphic phantoms of the foot and head to represent treatment sites on the ankle and nose. The areas to be treated, or "tumours", were outlined using Beekley Medical CT tape (Varian Medical Systems, Palo Alto, CA) to ensure proper applicator coverage after scanning.

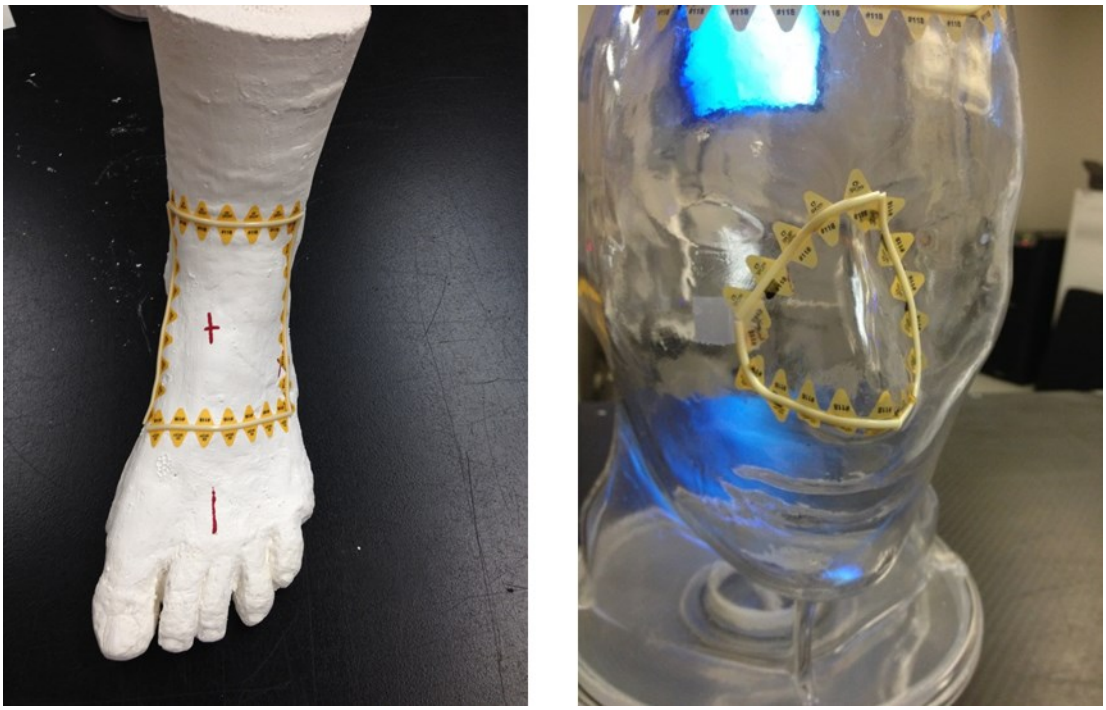

Figure 17 - Left: Foot phantom with ankle tumour outlined. Right: Head phantom with nose tumour outlined.

2.1 Creating Surface Applicator

The process of applicator design began with a CT scan of the phantom on a GE Discovery STE CT scanner (GE Medical Systems). The final resolution of the surface applicator depended on the resolution of this initial CT series, and for the phantom study,

was set to 2.5 mm slice thickness. The images obtained were axial cross-sections representing the anatomy of the phantom, which simulated a clinical patient. This allowed planners an inside look at locations of diseased area and normal tissue. The head phantom was scanned using a C-Silverman headrest held in place with the Uniframe thermoplastic mask system. The scan was performed in the supine head-first position. The foot phantom used similar settings and was scanned in the supine feet-first position. Once completed, the image series was imported into Eclipse Treatment Planning System (Eclipse version 11.0, Varian Medical Systems, Palo Alto, CA) for applicator design.

The surface applicator, required to hold the radioactive source in place using 6-French after-loading catheters (2 mm in diameter), needed to be thick enough to house the source at an appropriate distance to adequately irradiate the surface. The initial phantom study was designed as a comparison between two applicator modalities: Freiburg Flap (FF) applicators were used as a control, and the novel method of 3D printed applicators was used to compare. In order to assess the efficacy of the new 3D printed method, the number of variables between the methods should be minimized. Since the FF sheets are constructed of 1 cm diameter silicone spheres with a predrilled tunnel passing through the centre, a fixed source to treatment plane distance of 5 mm was used for the 3D printed applicator. The entire thickness of the applicator was set at either 1.5 or 2 cm to ensure there would be enough space for the generation of catheter tunnels.

Once in Eclipse, the applicator was created using the margins outlined by the CT tape on the surface of the phantom, representing the size and location of the tumour to be treated. In order to achieve complete coverage, the applicator was made to be about 2 cm larger than the delineated tumour in all directions. The creation of the applicator, as well

as its size relative to the treatment site, can be seen in Figure 18. This Eclipse-generated applicator was exported as a stereolithography (.stl) file to be customized and printed. An additional optional step could be taken to smooth the applicator before customization, however in doing so, there is a decrease in resolution that could result in the applicator not forming as tight a fit to the phantom (or patient).

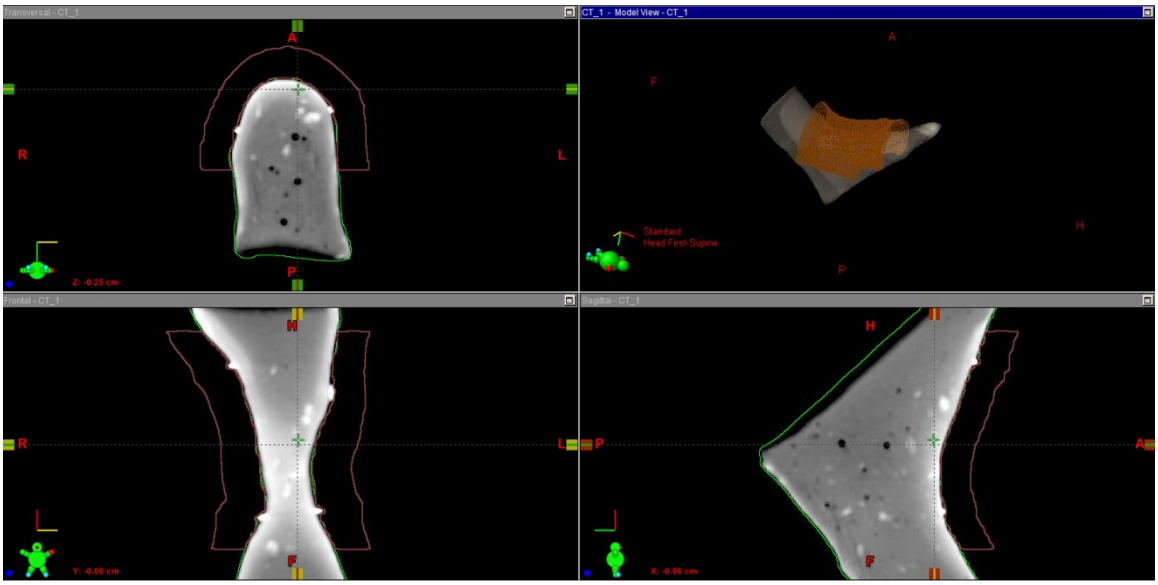

Figure 18 - Creating the applicator in Eclipse. White points on the surface represent CT tape delineation of the tumour.

The .stl file was imported into the 3D modeling software Blender (an open-source 3D computer graphics software). The process of obtaining a functional and printable applicator was acheieved in two steps. First, the bottom of the applicator needed to be perfectly flat to ensure it would sit evenly on the print bed. This was done by intersecting the bottom of the object with a plane created in Blender and subtracting the intersecting points. The second step in the customization process was to design tunnels for the insertion of catheters into the applicator. They needed to be sufficieintly large enough to hold the 2 mm afterloading catheters in place without moving. Their purpose was to

allow the radiation source to travel freely within the applicator to each dwell position to deliver dose. The tunnel was made by creating a cylinder that followed the contours of the applicator such that the centre of the cylinder remained 5 mm from the treatment surface. The diameter of the cylinder needed to be large enough to comfortabley fit a 6-French flexible after-loading catheter without kinking, yet small enough to not move around within the applicator. The ideal diameter for the cylinder was found to be 3.3 mm. Once the whole cylinder was created, a subtraction operator was performed to remove the interesting points within the applicator, creating a tunnel in a similar way to the first step that flattened the bottom. The process was repeated, separating each cylinder by an inter-catheter distance of 10 mm (the diameter of the FF spheres), until the entire applicator was fitted with tunnels.

The 3.3 mm ideal diameter was found experimentally by first measuring the diameter of a 6-French after-loading catheter. The second step was to print an object with varying diameter tunnels printed inside to assess the fit. If the tunnel had no curves, the catheter would easily slide into place without kinking, however, once a realistic applicator was made with curves that resemble a patient, the diameter needed to be increased. If the catheter were to kink during the insertion process, it could result in the source getting stuck and not being able to proceed to its desired dwell position. This would halt treatment and result in the need for a new applicator.

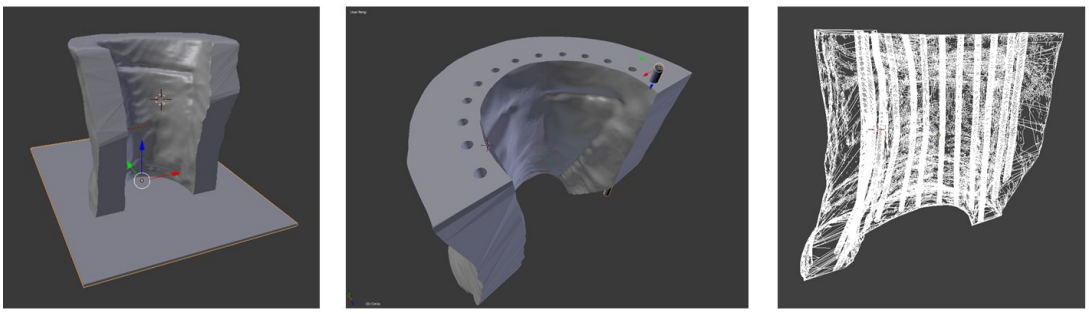

Figure 19 - Blender images showing applicator customization. Left: Bottom cropping. Middle: Tunnel creation. Right: Final applicator fitted with tunnels, showing wireframe image.

The final applicator, fitted with catheter tunnels, was exported as an .stl file, providing the necessary input to the 3D printer for fabrication. The applicator was printed on a Lulzbot Taz 5 (Aleph Object Inc.) using Ninjaflex, a type of flexible printing filament. Ninjaflex is a specially formulated thermoplastic polyurethane material providing flexibility and longevity when compared to traditional 3D printing filaments (27). The flexible filament, when compared to more rigid printing filaments, allowed for easier fitting due to its pliable nature. It could be temporarily deformed to avoid irregularities before settling back to its original shape. Within the printing software, the applicator was oriented such that the cropped flat bottom was in contact with the build plate. Once the object was in the correct orientation, parameters such as percent infill, layer height, and speed needed to be determined. The layer height controls the thickness of deposited filament in each layer determining the resolution of the object. A smaller layer height would correspond to a smoother object. The layer height for the applicators presented in this study was set to 0.2 mm. The speed corresponded to the speed of the extruder in the x-y dimension. Different filament materials can support different extruder speeds. Due to the flexible nature of Ninjaflex, a lower print speed is required to achieve a successful print, giving the filament time to cool and solidify before another layer is

printed on top. It was noticed that any speed higher than 30 mm/s caused the print to fail before completion. To ensure print success, the speed was set to its lowest setting, 18 mm/s, which resulted in an increase in print time, but had far fewer print failures. The infill parameter is what affects the print time and the characteristics of the applicator the most. It is a parameter that governs how densely the object would be printed and whether it will be filled linearly or in a pattern (such as a honeycomb structure). 100% infill was used to create solid applicators. The CT value of a 3D printed object was previously measured to be 130 ± 20 HU, corresponding to a density of 1.119 ± 0.012 g/cm^3 (23).

In the early stages of this experiment there were several challenges in order to achieve a successful print. As mentioned above, if the section of the applicator in contact with the build plate was not perfectly flat, the object would lose contact and fail. Another problem that consistently arose was the clogging of the printer's extruder. Initially this was believed to be a temperature related issue, however once the proper temperature was set, the clogging continued. After a great deal of research and hypothesis testing, it was found that a setting within the printer specifications needed constant adjustments before each print. "Esteps/mm" is a setting that calibrates the feed of the filament exiting the extruder. This setting allows one to adjust how much filament can be fed into the machine. For example, if the software setting is to print 10 cm of filament, and 12 cm enters the extruder, there is a discrepancy that will result in a clog (more filament is entering than exiting). The Esteps/mm setting can be raised or lowered to adjust this difference and ensure that the amount of filament entering the extruder is the same as the amount exiting. Adjustment of this setting was carried out before each print by marking off 12 cm of filament above the extruder and changing the printer setting to extrude 10

cm. Upon remeasuring where the initial mark was, if there was any value other than 2 cm, the Esteps/mm needed to be adjusted. This process was repeated until the extruding filament was equal to the entering filament. Once this step was added to the beginning of each print, the failures as a result of clogging stopped immediately.

2.2 Tunnel Automation

At the start of this project the process of fitting the applicator with tunnels was done manually, with each tunnel being placed one by one. A novel in-house algorithm was developed using Blender to create the tunnels programmatically. Similar to the method previously described, the bottom of the applicator needed to be smoothed to ensure contact with the print bed. It is also important at this step to check that the applicator is in the proper orientation to be printed. The algorithm is described below.

Step 1 – The first step of the algorithm is a manual process of selecting the two lateral limits on the applicator where tubes can be created. This is accomplished within the Edit mode in Blender and by clicking the desired points to represent the limits of the tunnels.

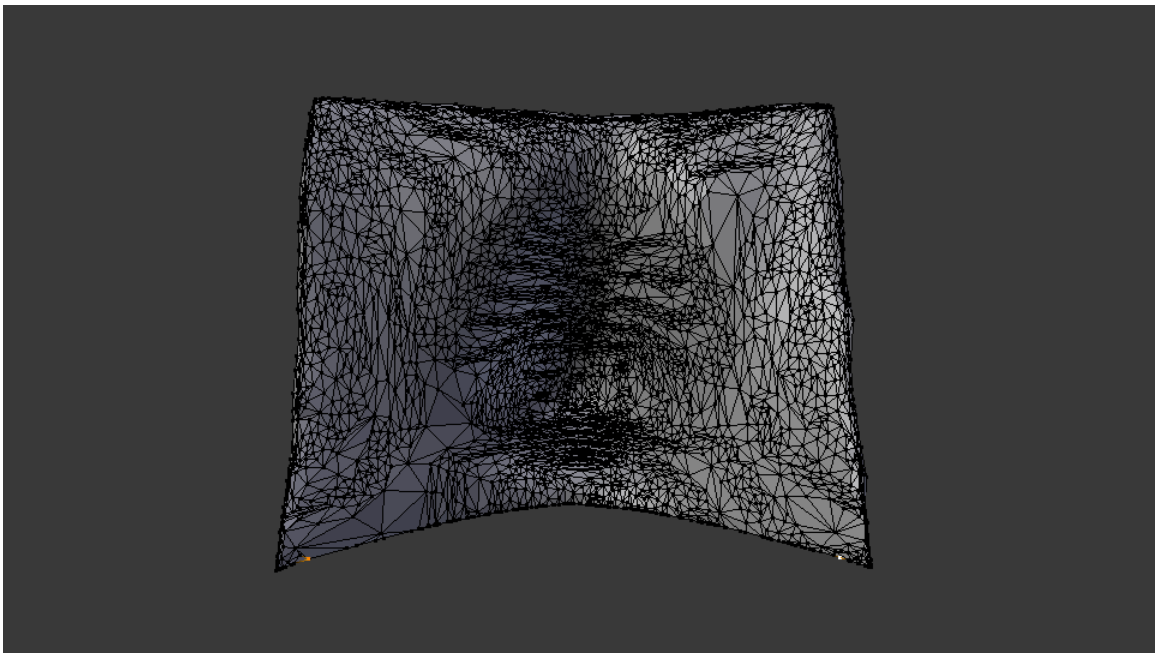

Figure 20 - Selecting the outer limits of tunnels to be created by the algorithm indicated by the two highlighted points on the inferior side of the applicator.

Step 2 – The algorithm then selects the bottom 5% of the object as a means to detect the side of the applicator that will be in contact with the patient. The proximal side (side touching the patient) is selected based off the normal vectors of each point. This step results in the selection of the bottom edge of the applicator in contact with the patient.

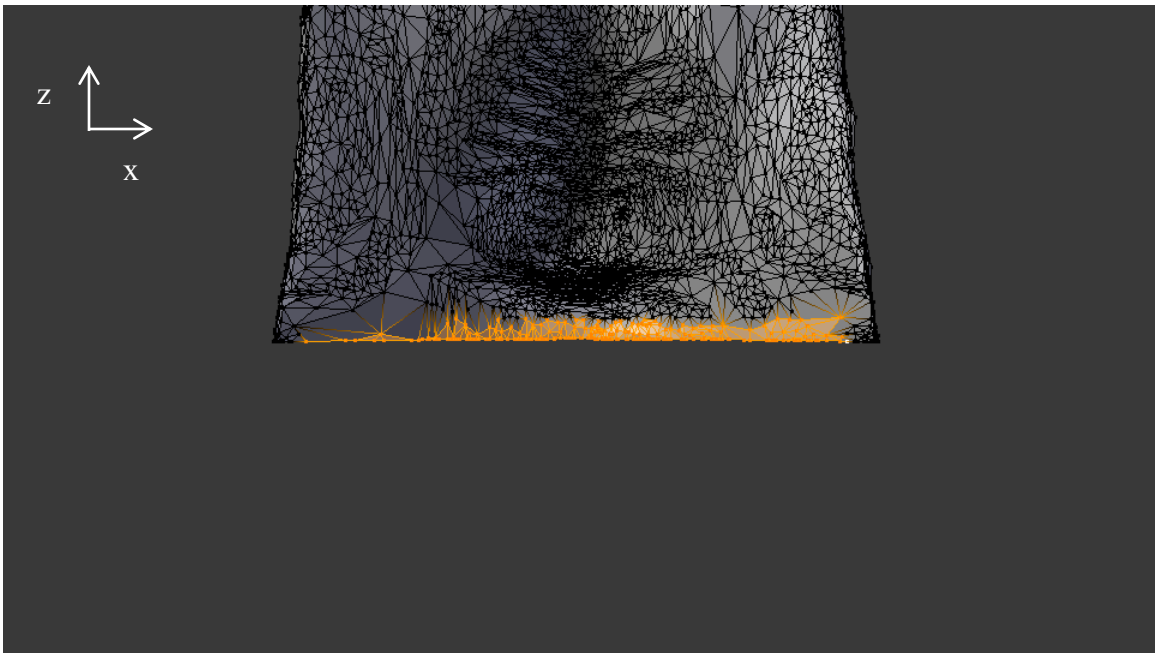

Figure 21 - Bottom 5% of points selected by the tunnel creation algorithm, bound by the two selected points from Step 1.

Step 3 – Once the proximal edge is obtained, a distance calculation is performed in order to find the inter-catheter spacing. It is accomplished by starting with the centre of the object and moving to the right towards the limit selected in Step 1, performing a Euclidian distance to find the nearest point located at least 10 mm from the last point. The process halts when it reaches the point selected in Step 1 before repeating the process travelling to the left.

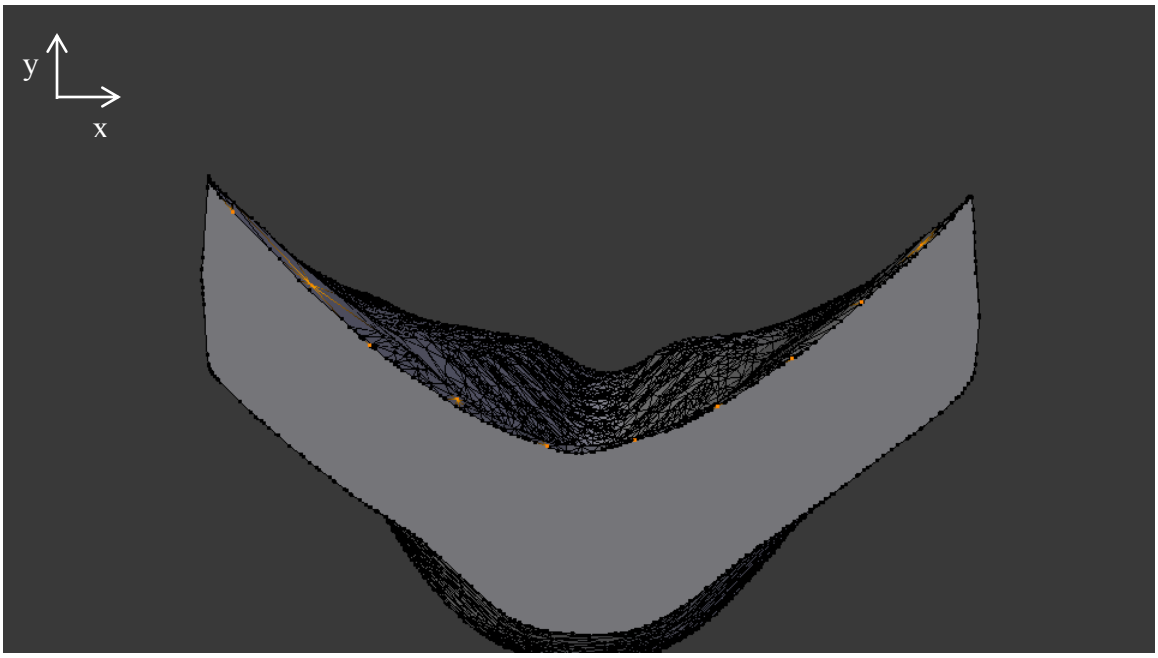

Figure 22 - View of the applicator showing the selected points where tunnels wish to be created.

Step 4 – Once the x-y coordinates of the tube locations are selected, the process of tunnel creation can begin. The first step is to sort the points such that they can be manipulated in a continuous fashion. A loop was generated to analyze the points one by one and perform the following steps:

a) A slice of the object was made using the x-y coordinates of the point obtained in the previous step with a margin of ±1 mm. The points within the overall mesh located within this slice were taken and placed in an array, represented as the highlighted points in Figure 23.

b) The mean value of the normal vectors to these points was calculated as well as the angle. The angle was used to rotate the object such that the normal vectors were all facing the y-direction.

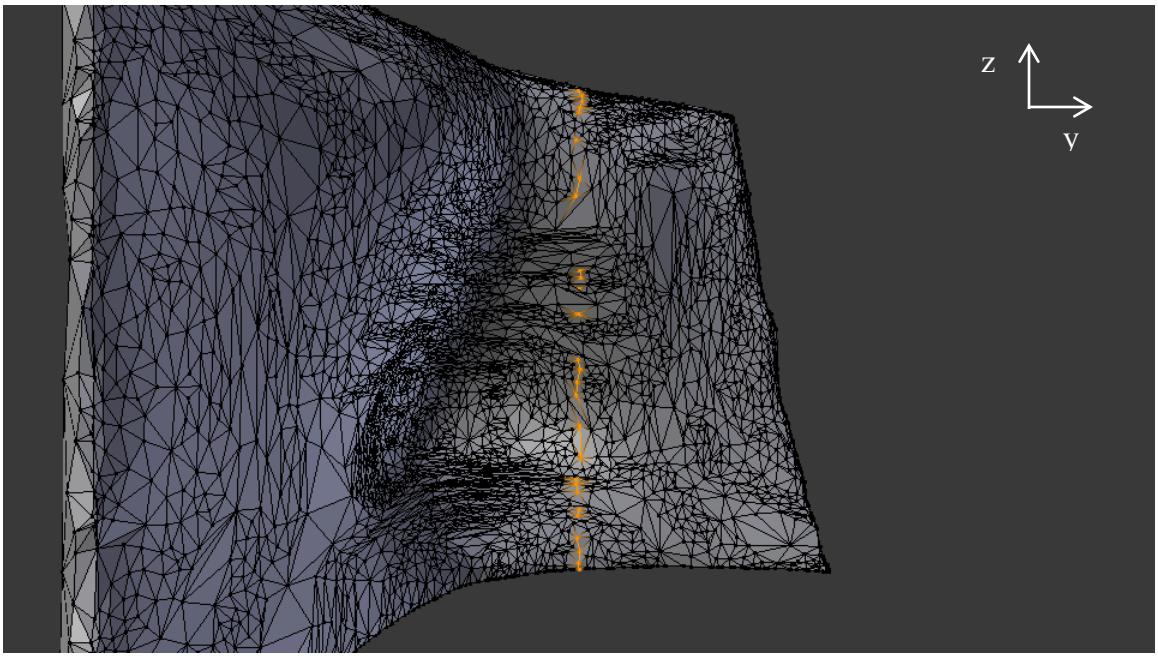

Figure 23 - Applicator showing highlighted points within a particular slice where a tunnel is desired. The applicator is rotated such that all the normal vectors are facing the +y-direction.

c) The objects points and normal values were extracted and saved in an array before the process was repeated for another slice.

d) Once all the normal vectors were saved in an array, only the normals with a +y-direction were chosen to ensure that only patient facing points were selected. The resulting points made up the basis for the tube.

e) The points were then moved 5 mm in the opposite direction of their normal vectors. This results in the tunnel 5 mm from the surface of the applicator.

f) Once the tunnel moved back, the top and bottom points were copied and assigned an extra 20 mm in the z-direction to ensure the tunnel would pass completely through the applicator.

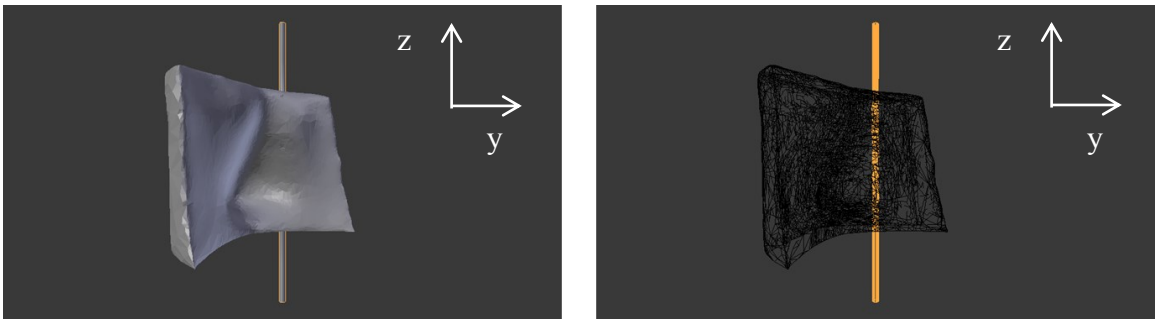

Figure 24 - Tunnel creation from Blender showing a solid view and a wire frame view with the tunnel highlighted.

g) The tunnel was created in Blender as a Bezier Curve. This allows it to follow the contours of the applicator while keeping the inner diameter the same. Other catheter tunnel techniques were tested and it was found that the Bezier curve was able to hold its shape better around bends.

h) The tunnel is deleted using the Difference Boolean Operator, creating an empty space.

i) The process is repeated for each tunnel location

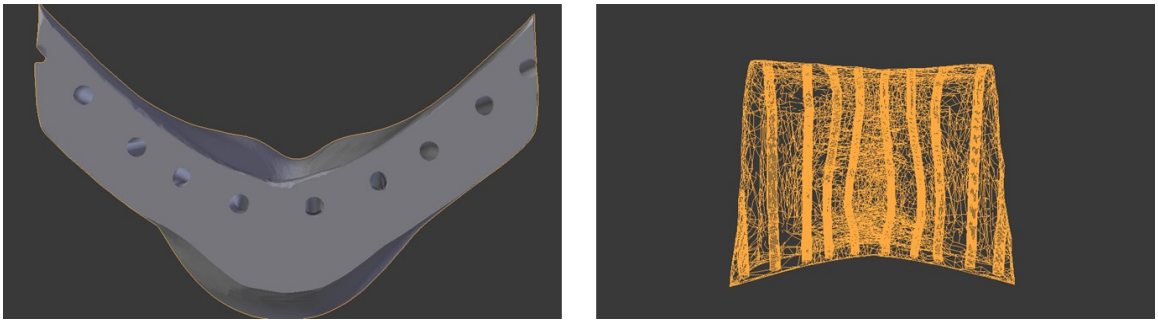

Figure 25 - Applicator fitted with computer generated tunnels using Bezier Curves. Left: Bottom view emphasizing location from the surface of the patient. Right: Wire frame showing the tunnels passing completely through the applicator.

Figure 26 – Programmed 3D printed applicator showing catheter tunnels for placement of radiation source.

2.3 Freiburg Flap Applicator Design

To compare 3D printed applicators to the status quo, an FF applicator needed to be constructed for both the foot and the nose phantom. A thermoplastic mesh was fitted to each phantom and allowed to set such that it followed the contours as closely as possible. Sheets of the flap material were cut to size, extending past the CT tape-delineated tumour by the same margins as the 3D printed applicator. For this study, instead of using sheets of flap material, individual strips were used to allow for better conformity. The strips were physically sewn onto the mask to make sure they would retain their shape, a rather time consuming process. The main objective was to minimize the distance between the flaps while conforming to the mask as much as possible. For certain cases this was easily done, as shown in Figure 27 for the foot phantom, however, for other regions it was much more difficult, such as the nose which has an irregular surface contour (Figure 28).

Once both applicators were constructed, they were fitted with 6-French after-loading catheters held in place by radiopaque buttons. Before being rescanned on the CT machine for treatment planning purposes, x-ray dummy sources were inserted into the catheters to represent the potential dwell positions for the source. These sources are radiopaque on the CT scan and allow the planner to reconstruct the catheters and first source position accurately.

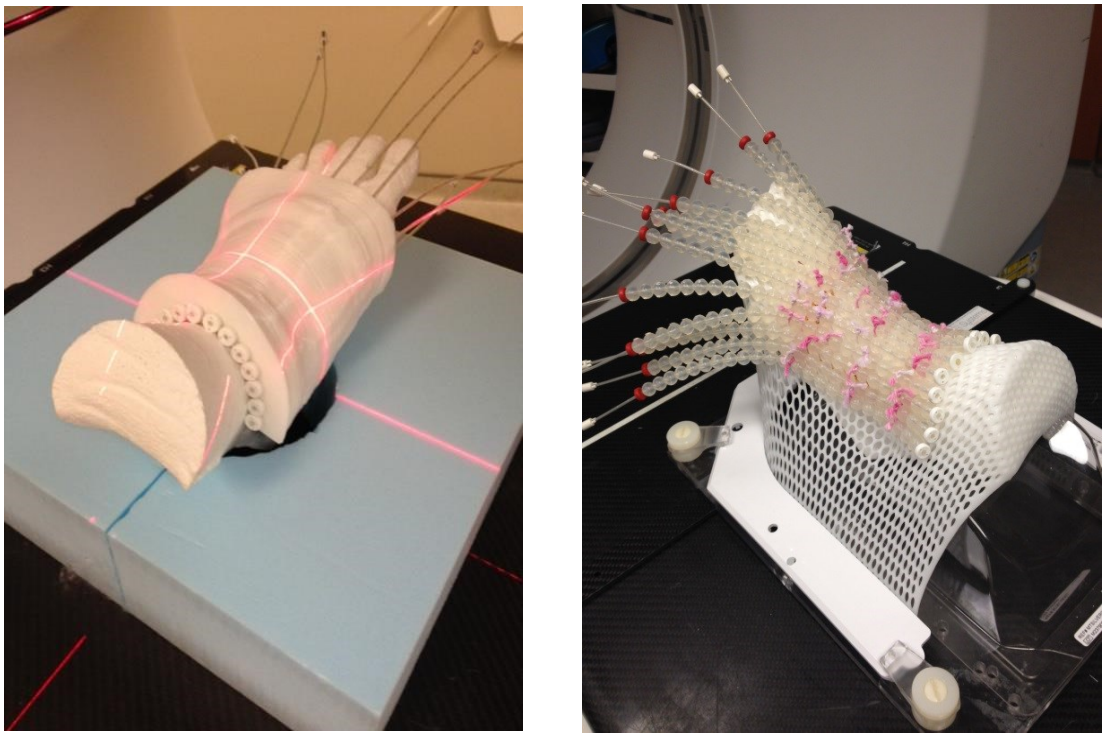

Figure 27 - Foot phantom fitted with Left: 3D printed applicator, Right: Freiburg Flap applicator.

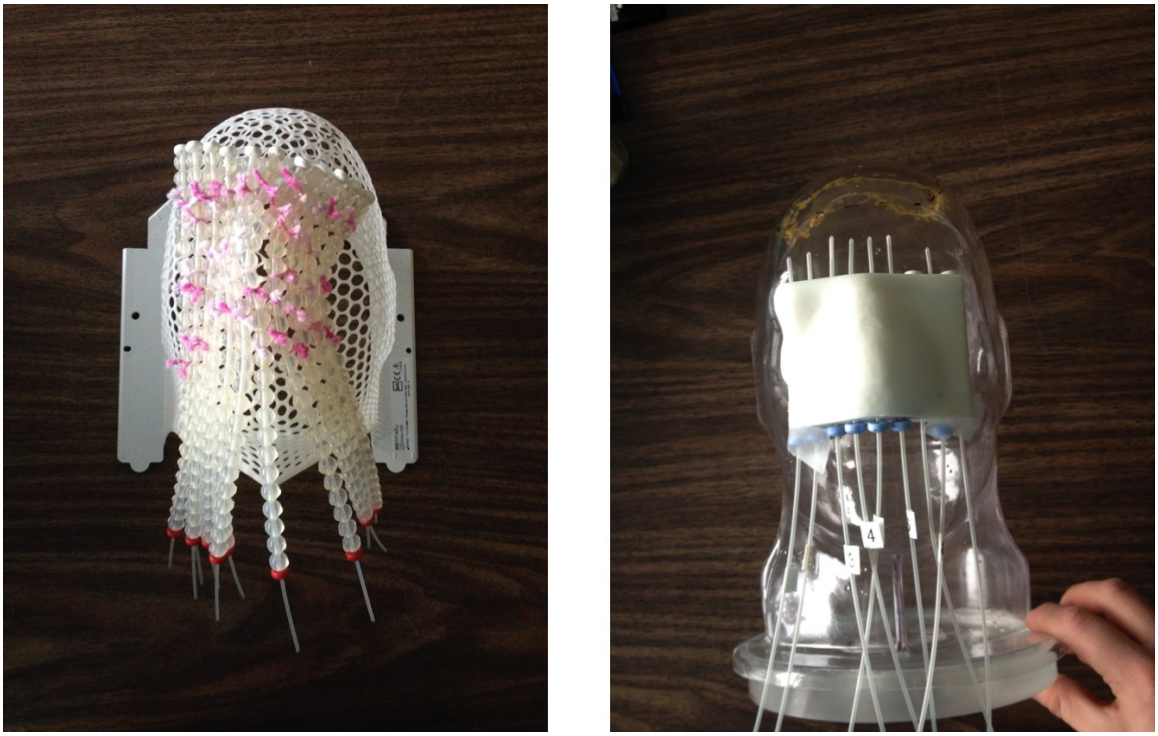

Figure 28 – Head phantom fitted with Left: FF applicator. Right: 3D printed applicator.

2.4 Measuring Source-to-Surface Distance

One of the primary concerns when dealing with brachytherapy plans is air gaps, further increasing the SSD. The radiation from the source is governed by the inverse square law (28). Applicators are made in such a way as to allow the steep fall off of the dose curve to occur in the applicator itself, allowing for more homogeneous dose to be delivered to the patient (see Figure 29). The addition of a mask to the FF applicator increases the distance between the source and the treatment plane, decreasing the amount of control a planner has over the resulting plan. A measure of quantifying the SSD was determined by examining the CT image series in Eclipse and contouring the space between the applicator and the surface of the phantom (25). Both FF and 3D applicators were set to a window/level threshold used for lung images. This was to ensure that only the distance between the distal side of the applicator and the proximal side of the

phantom were being contoured. Once the gap between source and surface was fully contoured, the volume of the structure was measured to determine the volume of the air gap. Due to the different sizes of the flap and the 3D printed applicator, only the air gaps corresponding to the area of the PTV were measured.

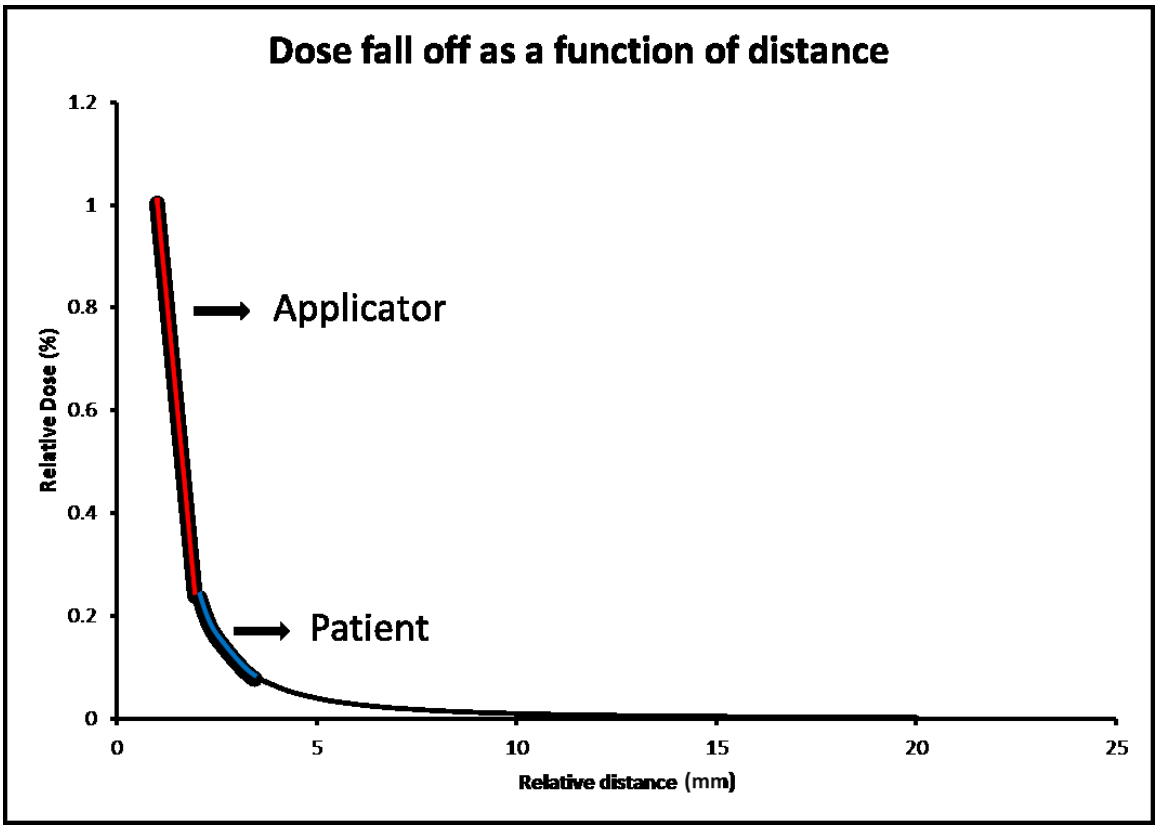

Figure 29 - Graph showing the inverse square law effect of the radiation source. The steep, high dose region occurs within the applicator while the more homogeneous portion treats the patient.

2.5 Creating Treatment Plan

The treatment planning software currently being used at the Nova Scotia Cancer Centre is Oncentra Brachy version 4.5.1 (Elekta). Once the phantoms were scanned with the applicators in place, the image set was sent to Oncentra for planning. Using the CT tape as a guide, the CTV was contoured 6 mm into the skin from the surface. This depth was chosen to simulate a clinical patient with a tumour penetrating the surface by 6 mm. One slice at a time, the region in between the CT tape was delineated to represent the

treatment volume. This is also the step where the OARs would be contoured if this were a real patient. The catheters were reconstructed one at a time from the x-ray dummy sources inserted before the CT was obtained. Starting with the first dummy position, the images were examined slice by slice until all of the potential dwell positions were generated in the planning software. An image of the contoured CTV, as well as a view of the x-ray dummy sources can be seen in Figure 31. The process of contouring the CTV and reconstructing the catheter positions was repeated as described for the FF applicator.

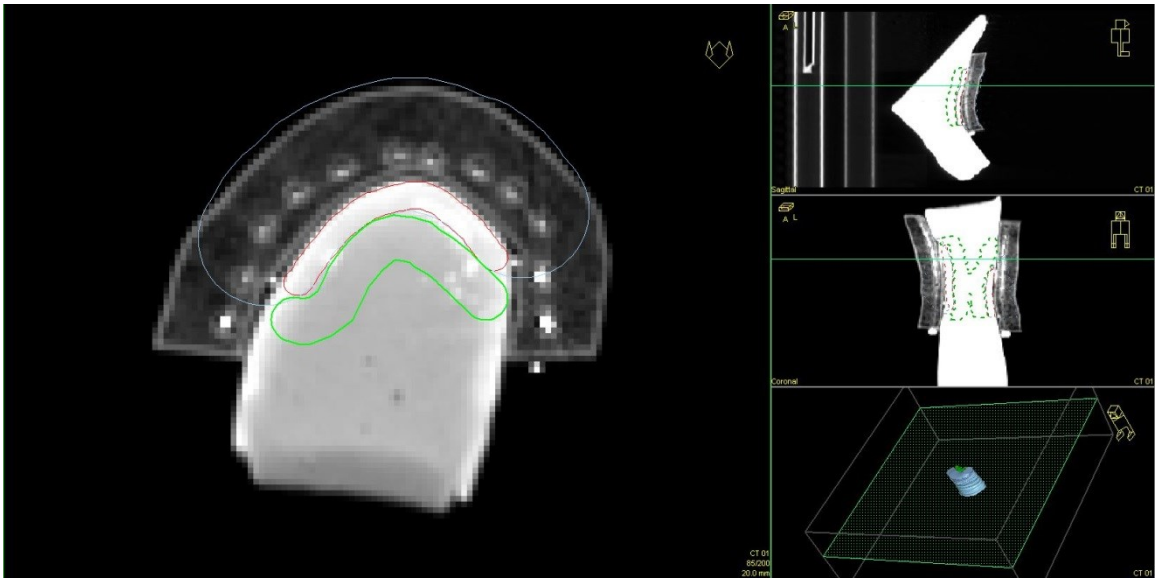

Figure 30 - View of the contoured CTV (red), an OAR (green), PTV (white), and the x-ray dummy sources within the 3D printed applicator in Oncentra Brachy.

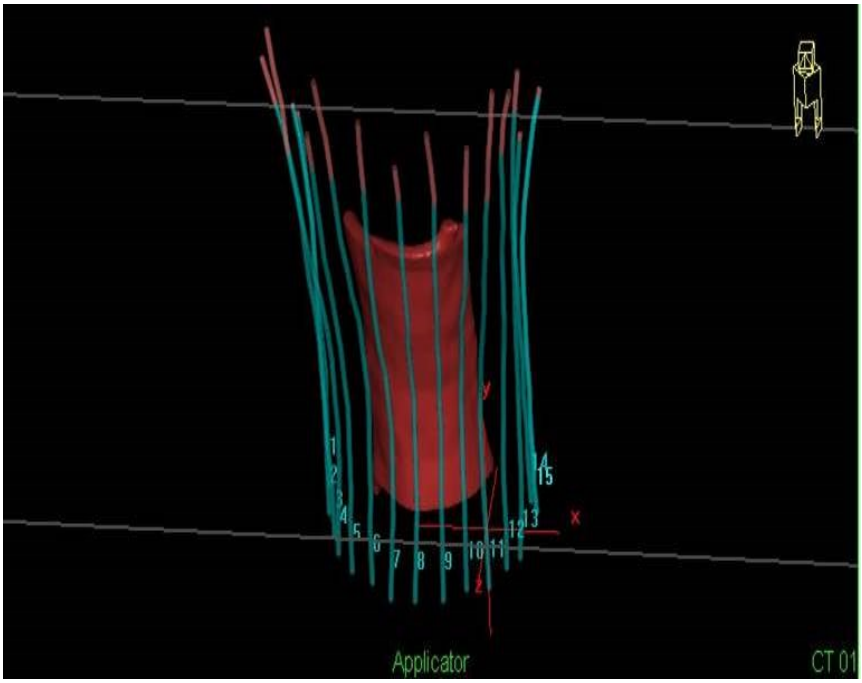

Figure 31 - Oncentra Brachy reconstruction of the catheters and the CTV (red) for the tumour on the foot.

2.5.1 IPSA Optimization

Once the CTV was contoured, a dose distribution could be generated from the planning software. As mentioned in Section 1.6.1, the dose optimization for this study was done using the IPSA algorithm, for which one provides as input dose-volume clinical objectives and the software works to ensure that the plan meets those objectives. For both the foot and the nose phantoms, the maximum dose was set to 450 cGy while the minimum dose was set to 300 cGy. The source step size for each plan was 5 mm. The normal tissue surrounding the tumour was given a max dose of 250 cGy.

In order to optimize using IPSA, a new structure was contoured to treat to the same depth as the CTV, but also extended outside the surface of the phantom such that the sources were contained within this new structure. This was done because IPSA can only activate the dwell positions within a given treatment structure for optimization (20).

Referring to Figure 30, the treatment volume is the structure contoured in the dark red colour while the structure contoured for IPSA is the faint light blue line that extends outside the surface of the patient. A second structure was created below the treatment volume to assist in the IPSA optimization. This region acts as an OAR, limiting the amount of dose that extends past the deepest margins of the CTV. This was contoured as the tissue beneath the distal side of the CTV. The OAR structure is represented as the green line in Figure 30.

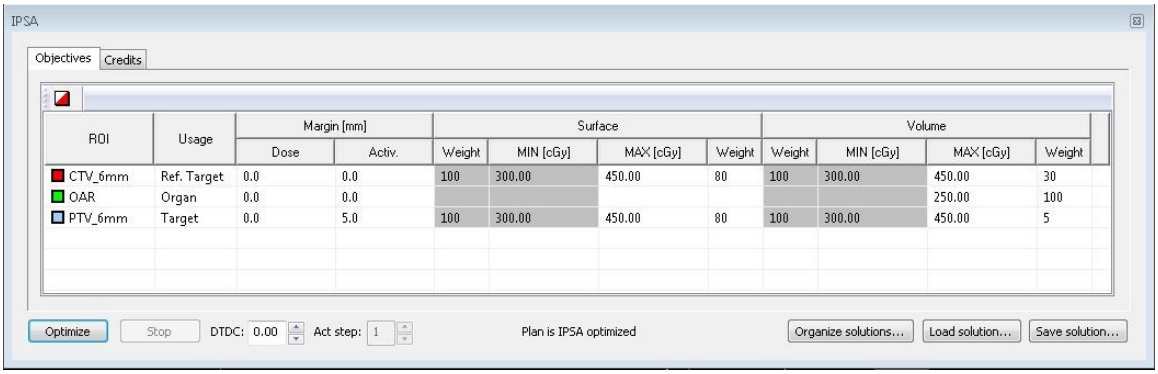

Figure 32 - Dialogue box from IPSA showing dose constraints to the PTV and OAR.

2.6 Data Collection

For both phantom cases analyzed, the dose distributions of the 3D printed applicator as well as the FF applicator were compared. One way to analyze a dose distribution is through DVH curves. Specifically, values were obtained that provide information about the amount of volume receiving a specific amount of dose, as well as the amount of dose delivered to a specific volume. The DHI, described in Section 1.6.1, provides information on the homogeneity of the dose distribution.

Table 4 - Defining relevant dosimetric parameters.

D_{90}	Dose delivered to at least 90% of the target volume
D_{100}	Dose delivered to at least 100% of the target volume
V_{100}	Percentage of volume receiving at least 100% of the dose
V_{150}	Percentage of volume receiving at least 150% of the dose
V_{200}	Percentage of volume receiving at least 200% of the dose

2.7 Clinical Cases

The quality of the approach used for the phantom study previously outlined has been successfully implemented in designing and printing of customized 3D HDR surface applicators for treating patients. The first patient to trial this method was a 74-year old male diagnosed with a basal cell carcinoma on his nose. As was the case in the phantom study, two sets of CT images were acquired with the patient oriented in the supine position, the first to design the applicator and the second with the applicator in place for treatment planning. The treatment area was outlined on the patient's skin using CT tape and scanned with 1.25 mm slice thickness for applicator design. This is higher resolution than was used for the phantom study to ensure that the applicator fit the highly irregular surface of the patient, and to retain as much resolution from the CT scan as possible. The process of applicator design followed the same procedure as outlined for the phantom study. Within Blender, it was desired that the centre of the catheter be placed 5 mm from the treatment surface, with inter-catheter spacing of 10 mm. This was challenging due to

the radius of curvature of the nose, so to ensure complete coverage, an extra catheter hole was designed to enter the anterior side of the applicator (this can be seen in Figure 33 by the radiopaque button entering from the side of the nose as opposed to the top).

At the time of the treatment planning CT scan, the patient was once again placed in the supine position with the 3D printed surface applicator in place, fully fitted with 6-French after-loading catheters. The CT scan was taken with 1.25 mm slice thickness and then imported into Oncentra Brachy for target volume and OAR delineation. The catheters were reconstructed with a 5 mm step size on the CT images and dose distributions were optimized using IPSA.

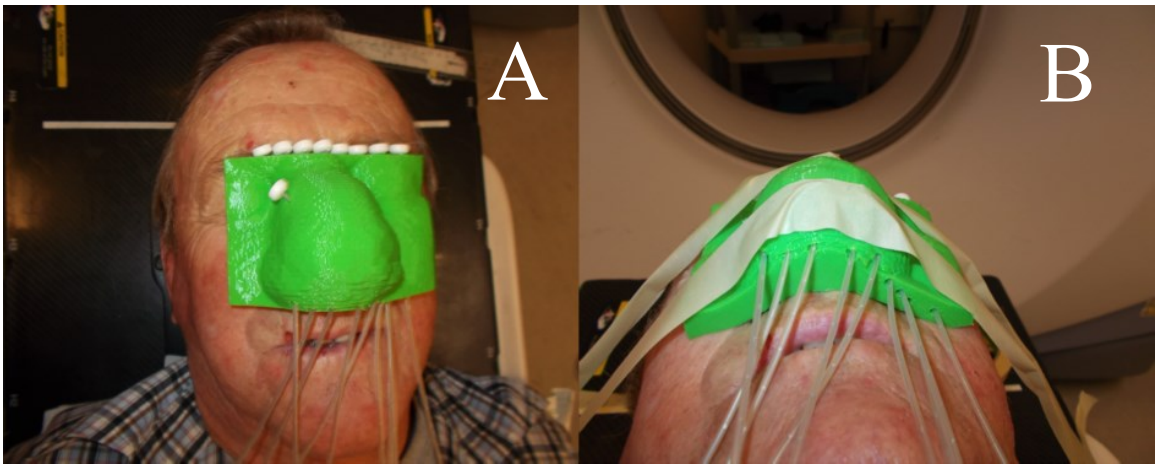

Figure 33 - 3D printed applicator designed for a patient at the Nova Scotia Cancer Centre with basal cell carcinoma of the nose. Images were acquired to assess fit and patient comfort.

The second patient to have an HDR brachytherapy applicator designed for treatment was a 17-year old patient who had developed a rare case of rhabdomyosarcoma in his soft palate. This applicator was unique in the sense that it was going to be going inside the patient's mouth as opposed to the surface of the skin. The patient was initially CT-scanned with a mouthpiece designed by a dentist, with 1.25 mm resolution to retain as much of the contours as possible. Within Eclipse, the mouthpiece was contoured and

exported to be customized within Blender. Due to the size of both the tumour and the mouthpiece, the applicator could only accommodate three catheter tunnels. Since this applicator was going to be in the patient's mouth and would occupy the majority of the oral cavity, an air hole needed to be incorporated. The air hole was created by intersecting a rectangular parallelepiped with the applicator in the same manner that was used to flatten the bottom, and removing the intersecting points with a subtraction operator. The process of tunnel creation, bottom flattening, and printing followed the steps outlined for the phantom study.

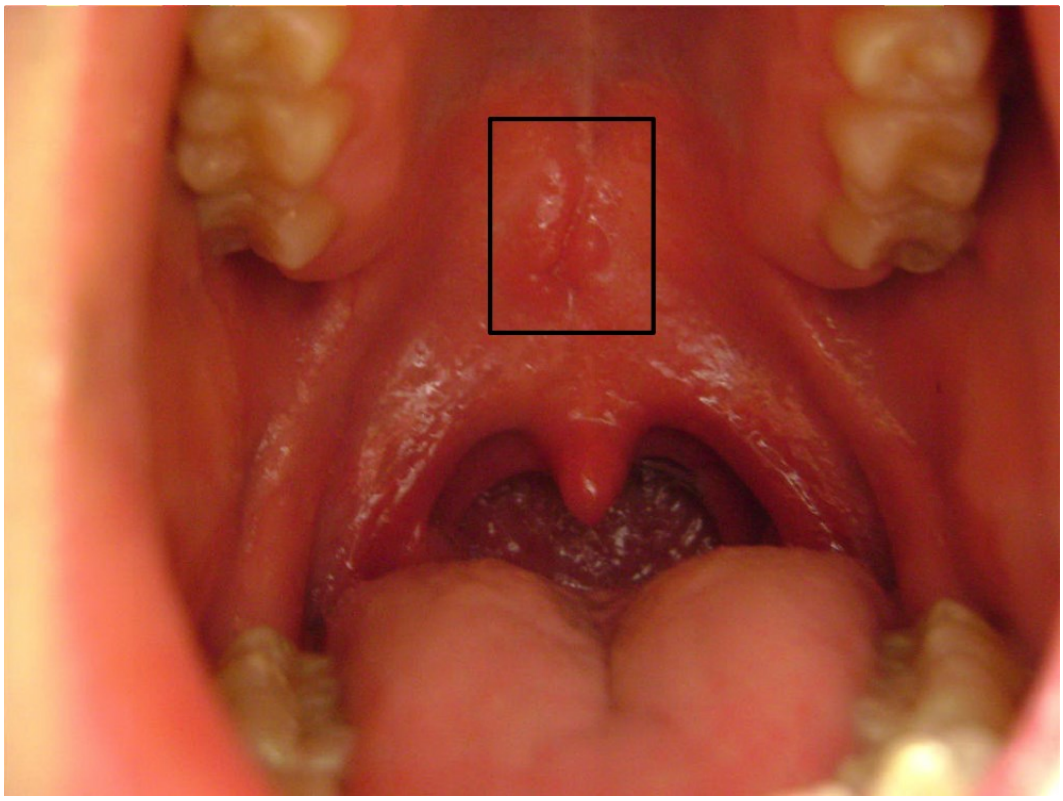

Figure 34 - Patient from the Nova Scotia Cancer Centre with rhabdomyosarcoma on the soft palate. Tumour is located within the black box.

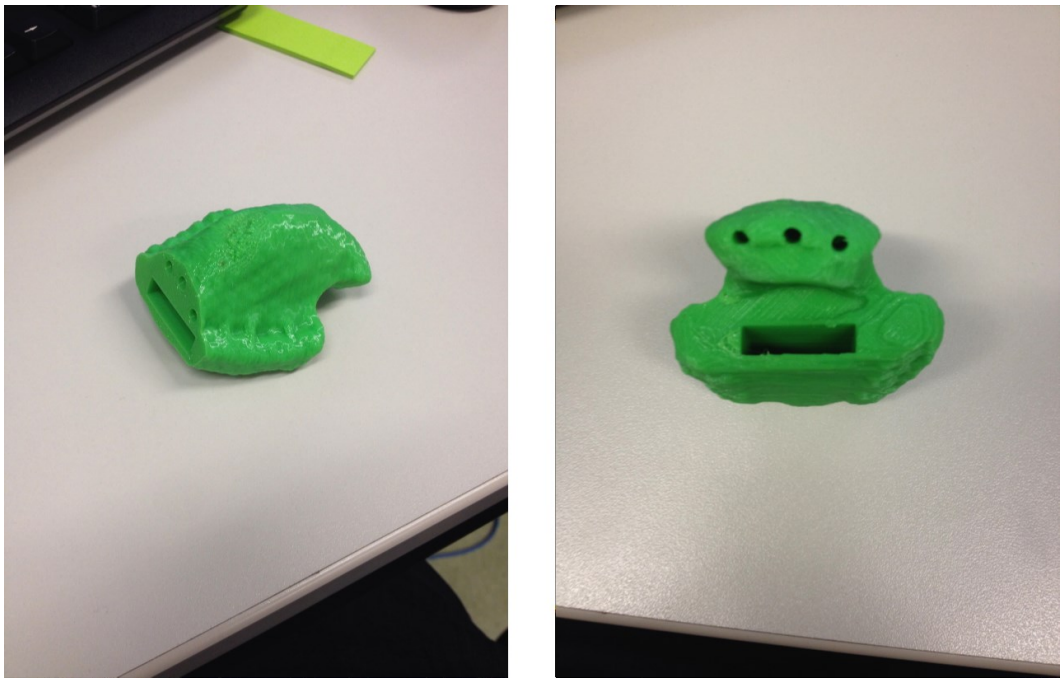

Figure 35 - Left: Side view of mouth applicator. Right: Top view showing catheter placement and air hole.

CHAPTER 3 RESULTS & DISCUSSION

3.1 Foot Phantom

The goal of the plan was to deliver the prescription dose to a depth of 6 mm below the surface of the phantom. The distributions for the Freiburg flap plan and the 3D printed plan are shown in Figure 36. For both applicator techniques, the dose distribution was optimized using the IPSA optimization algorithm. It can be seen that the 100% isodose line, represented in red, follows the contours of the PTV very closely. An OAR, shown in Figure 36 as the green dotted line located below the PTV, was contoured to measure the dose being delivered to the region surrounding the tumour. Analyzing the DVH curve for the CTV structures, shown in Figure 37, it can be seen that the dose distributions created for both plans are very similar. This was to be expected because for the relatively flat region of the ankle, a highly conforming Freiburg Flap applicator could be fabricated. Both applicator modalities registered a V_{200} of zero, indicating that all of the high dose regions for this plan occurred within the applicator itself. All of the dosimetric parameters listed in Table 5 show similar results for each type of applicator. The main differences come in the OAR sparing. For the 3D printed applicator, a lower mean dose delivered to the OAR is observed indicated the normal tissue is receiving less dose over the course of treatment.

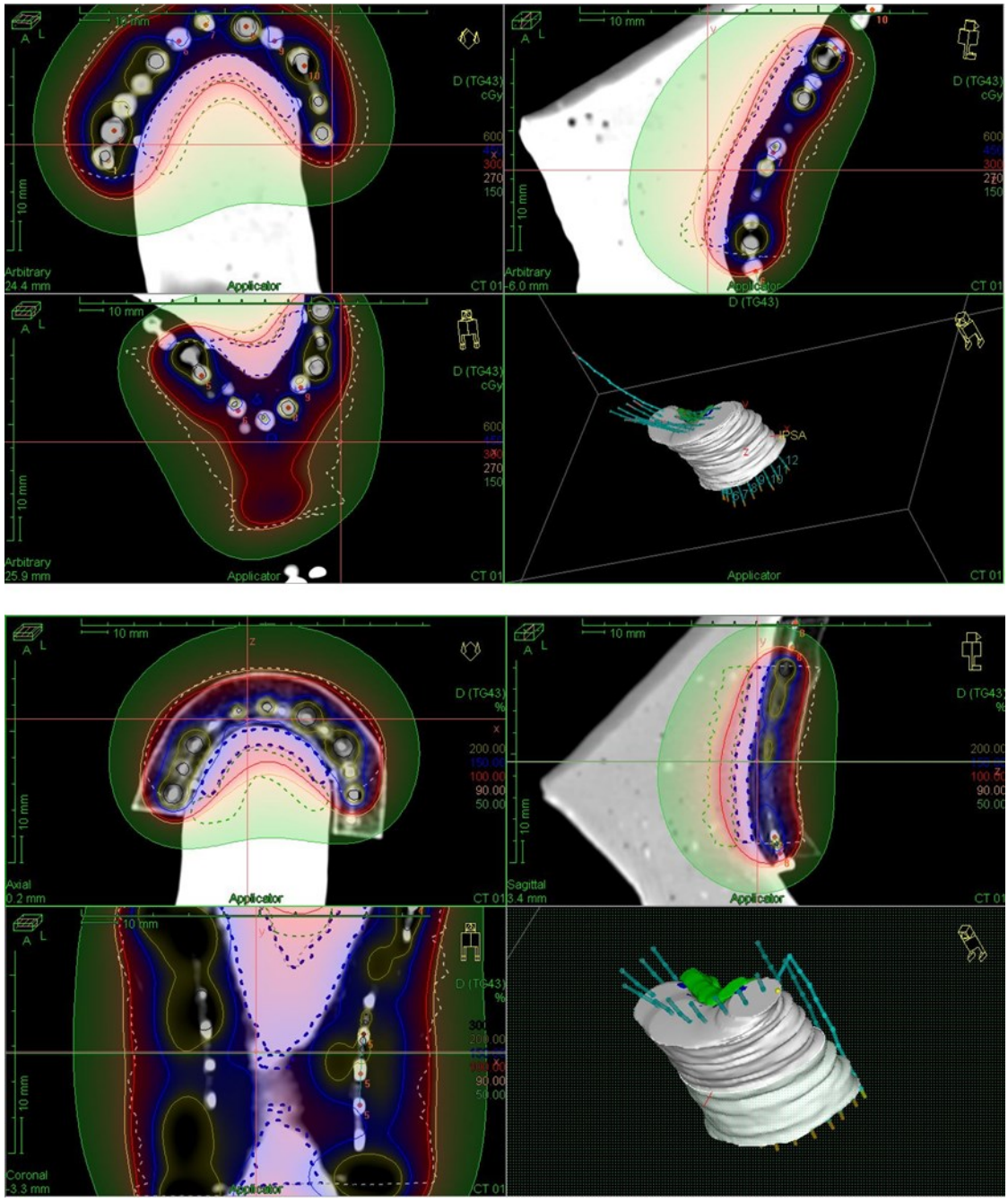

Figure 36: Dose distribution created for the foot phantom experiment. Top - Freiburg Flap. Bottom - 3D Print.

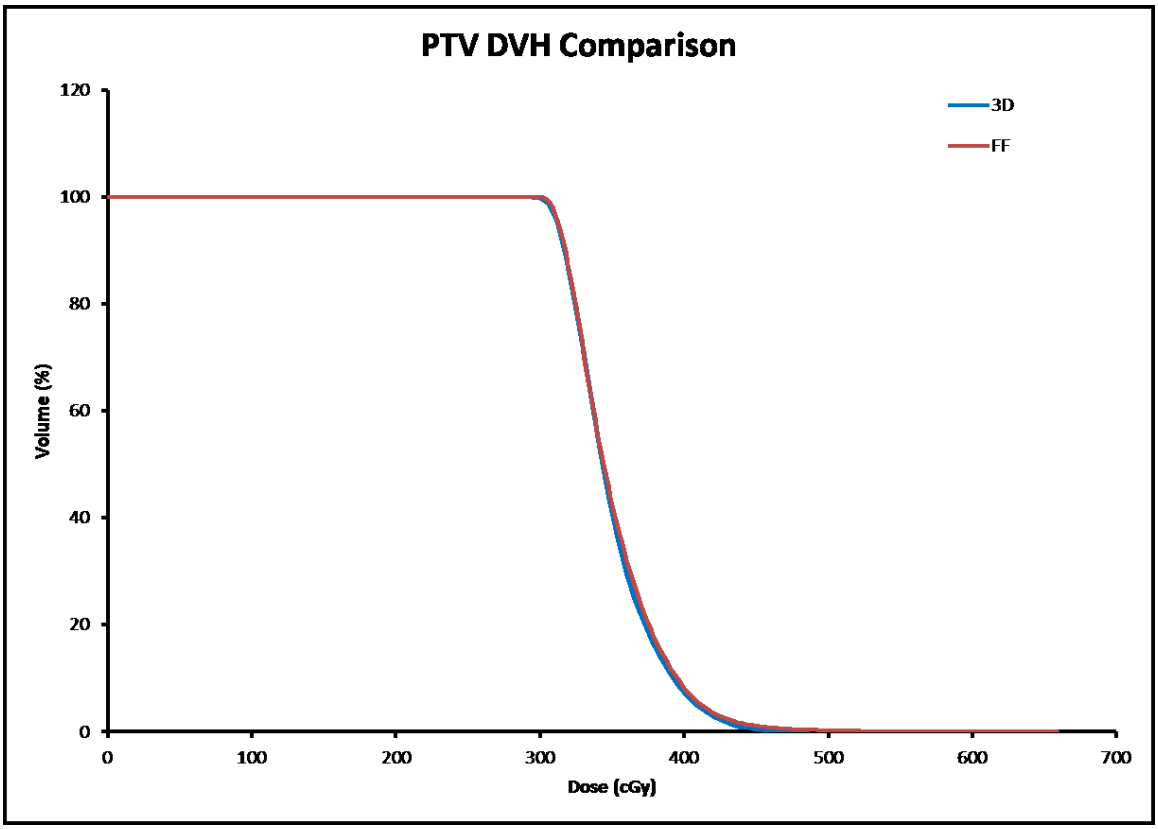

Figure 37 - DVH comparison of 3D printed applicator vs. Freiburg flap for foot study.

Table 5: Dosimetric parameters for foot phantom experiment.

	3D CTV (%)	3D OAR (%)	FF CTV (%)	FF OAR (%)
D_{90}	108.1	74.2	105.3	86.7
D_{100}	100.2	59.4	98.9	68.3
V_{100}	100.3	21.6	94.7	17.17
V_{150}	2.5	0.0	1.0	0.0
V_{200}	0.0	0.0	0.0	0.0
DHI	97.5		99.0	

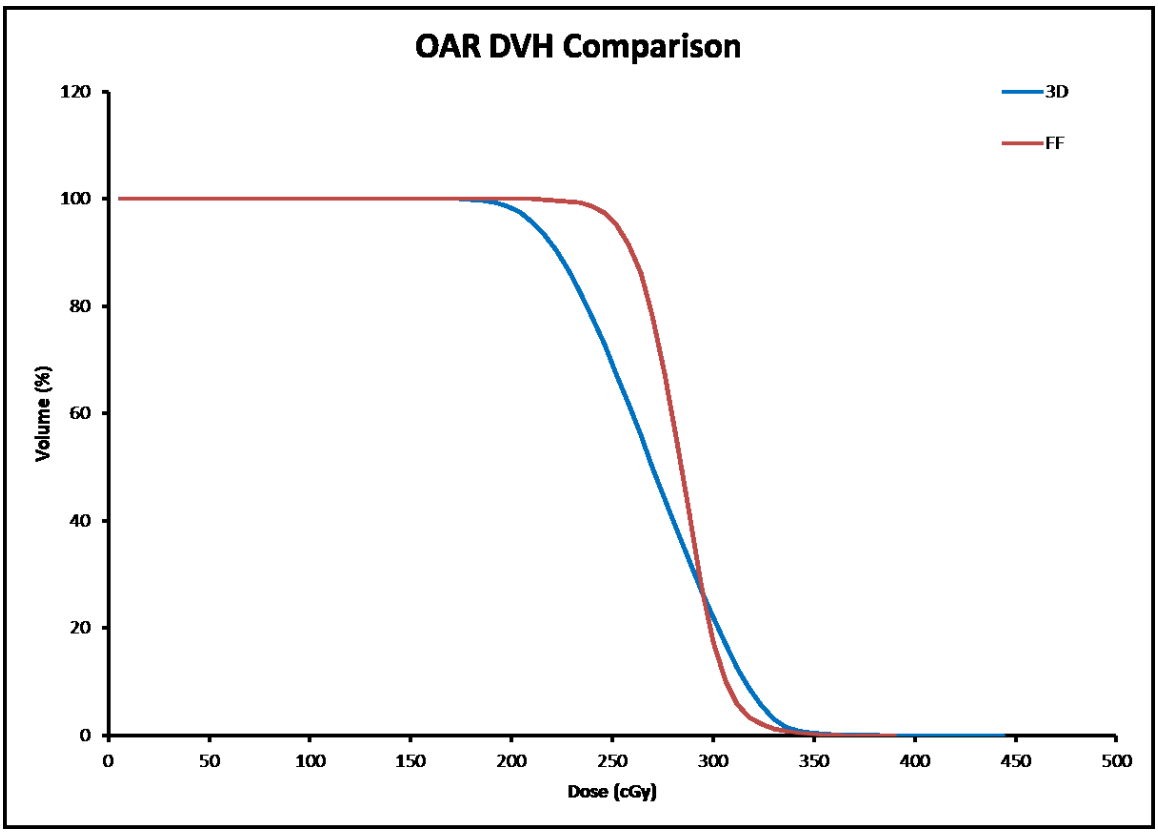

Figure 38 - OAR DVH comparison for the foot phantom study. The 3D printed applicator exhibits a lower mean dose to the OAR, indicated by the more gradual slope.

3.2 Nose Phantom

The experiment examining application to the nose yielded promising results for the 3D printed applicator technology. Similar to the foot experiment, the nose had a V_{200} value of 0 for both applicator types. The D_{90} and V_{150} improved by 4.2% and 29.2% respectively by taking a ratio of the two plans. Looking at the DVH curve in Figure 40, these improvements correspond to a sharper fall off for the 3D applicator. Similarly to the foot phantom study, an OAR (represented in Figure 39 as the green dotted line) was contoured posterior to the PTV to assess dose being delivered beyond the treatment volume. In both applicator techniques, there was a large amount of dose delivered to this OAR in order to achieve 100% prescription coverage of the PTV. This is due to the

proximity of the source to the treatment plane and the radiation from each dwell position being added together. This is not something that can be adjusted for when using a Freiburg Flap applicator but with a 3D printed applicator, if the plan does not provide adequate normal tissue sparing, the distance of each tunnel to the skin surface can be adjusted to result in a much more conformal dose distribution to the lesion. The value for DHI was slightly higher for the 3D printed applicator, indicating a more homogeneous dose distribution.

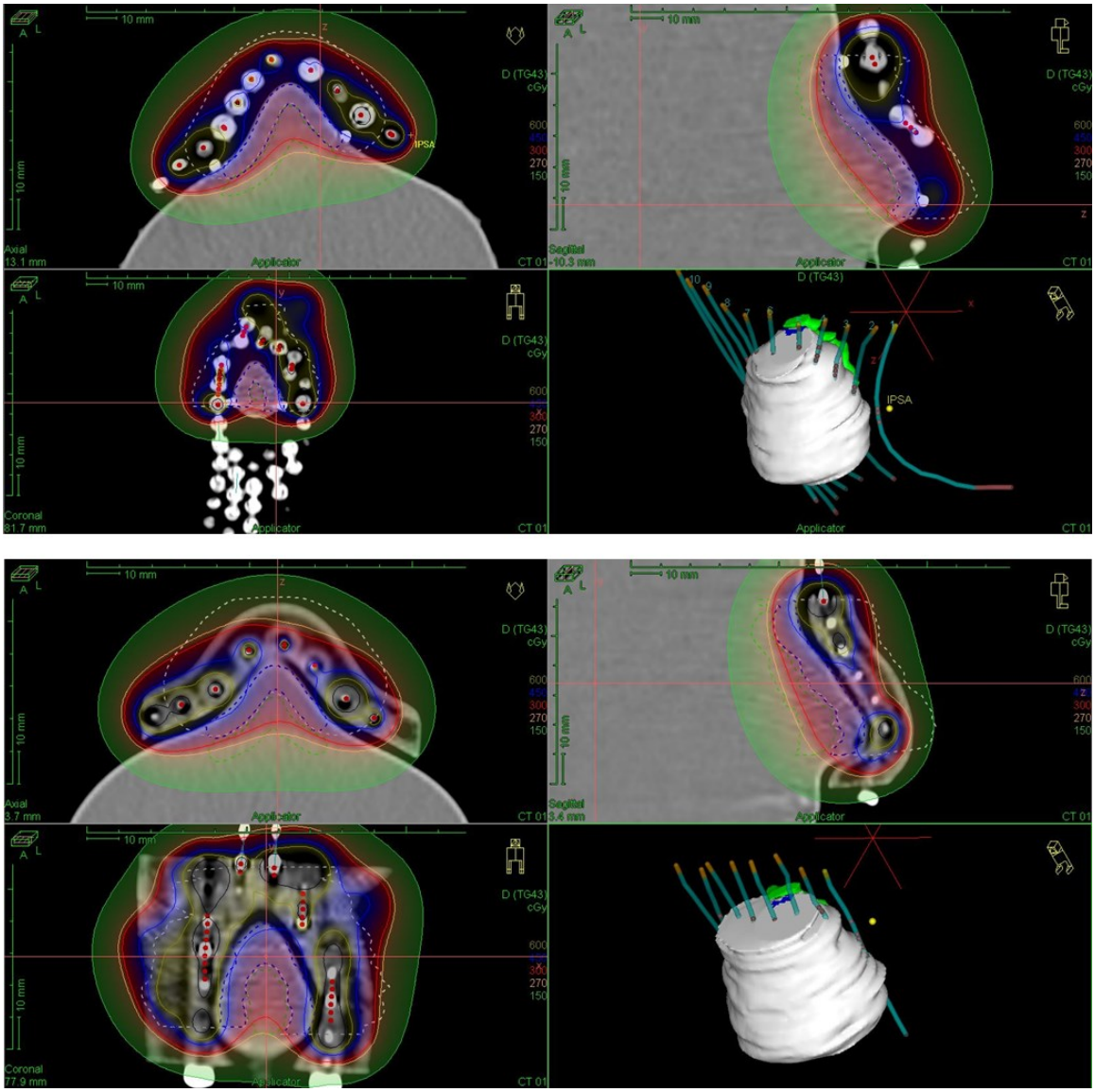

Figure 39 - Dose distribution created for the nose phantom experiment showing Freiburg Flap (top) and 3D printed applicator (bottom).

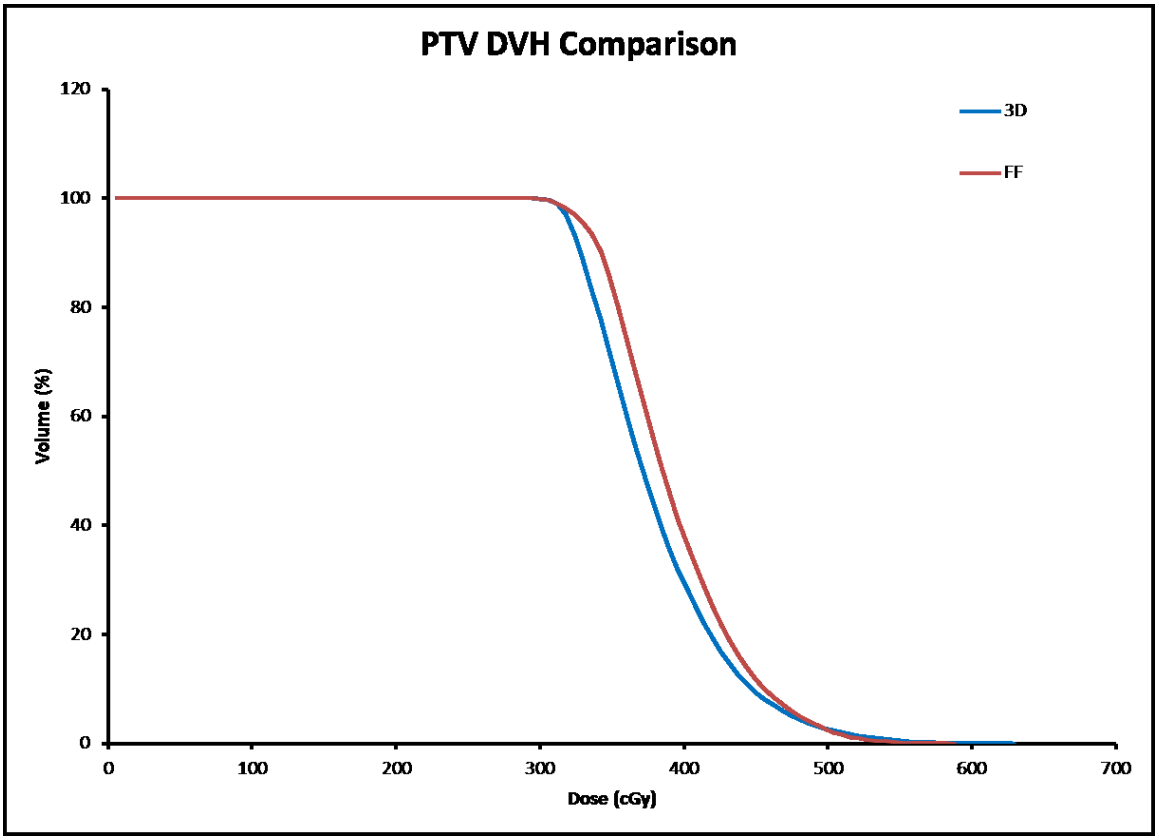

Figure 40 - DVH comparison of 3D printed applicator vs. Freiburg flap for nose study.

Table 6: Dosimetric parameters for nose phantom experiment

	3D CTV (%)	3D OAR (%)	FF CTV (%)	FF OAR (%)
D_{90}	109.5	80.1	114.1	78.1
D_{100}	100.0	69.5	99.9	64.6
V_{100}	100.2	32.4	99.7	32.1
V_{150}	9.2	0.0	11.9	0.0
V_{200}	0.0	0.0	0.0	0.0
DHI	90.8		88.1	

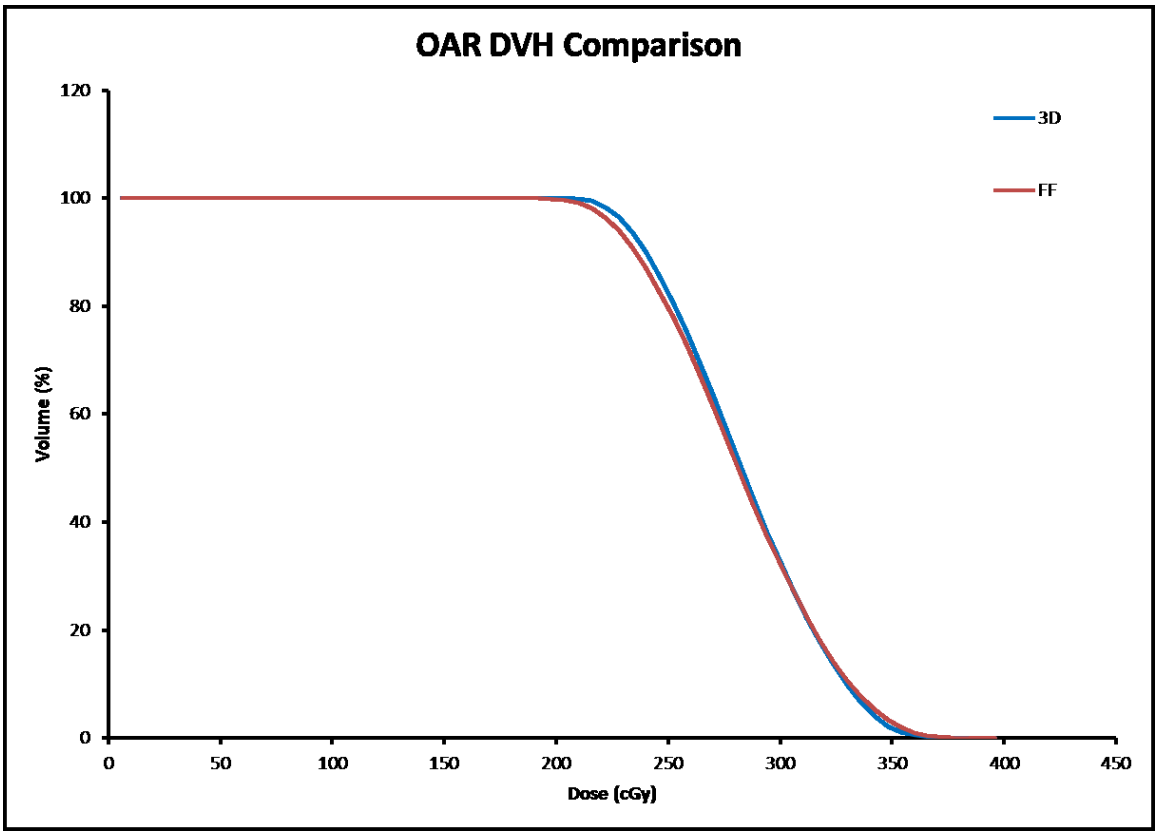

Figure 41 - OAR DVH comparison for the nose phantom study.

3.3 Air Gaps

The air gaps were assessed for both the study of the foot phantom as well as the nose phantom. Figure 42 and Figure 43 show the Eclipse contours created for the foot and nose study repectively, showing the difference in volumes of air between applicator and surface for the Freiburg flap and the 3D printed applicator. Table 7 shows the volumes found for each case, measured in cubic centimetres. In both experiments the volume dropped considerably from the flap to the 3D print. The foot phantom saw a 98% reduction in air gaps while the nose phantom dropped 58%.

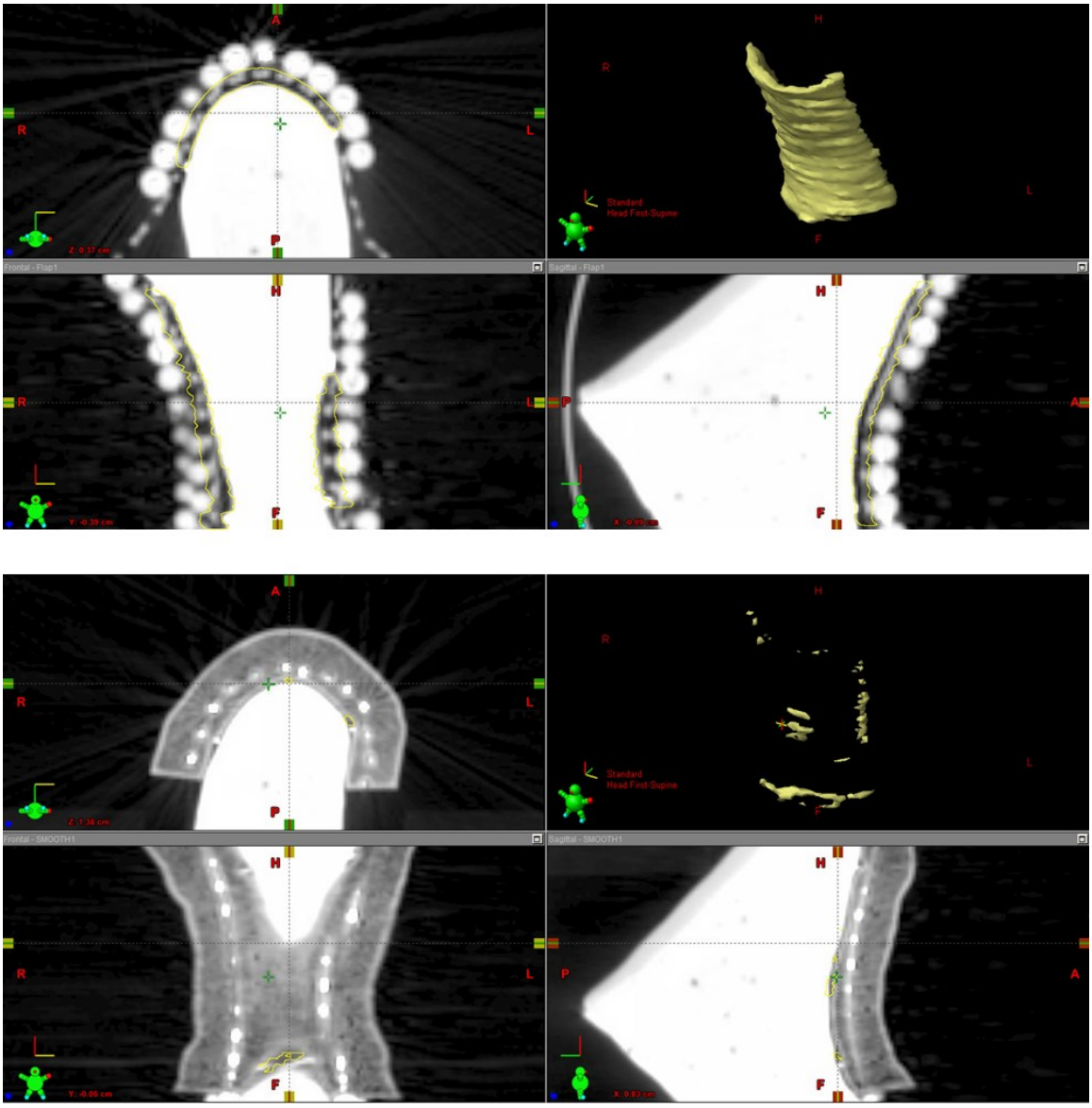

Figure 42: Contoured air gaps generated in Eclipse for foot experiment. Top: Freiburg flap. Bottom: 3D printed applicator.

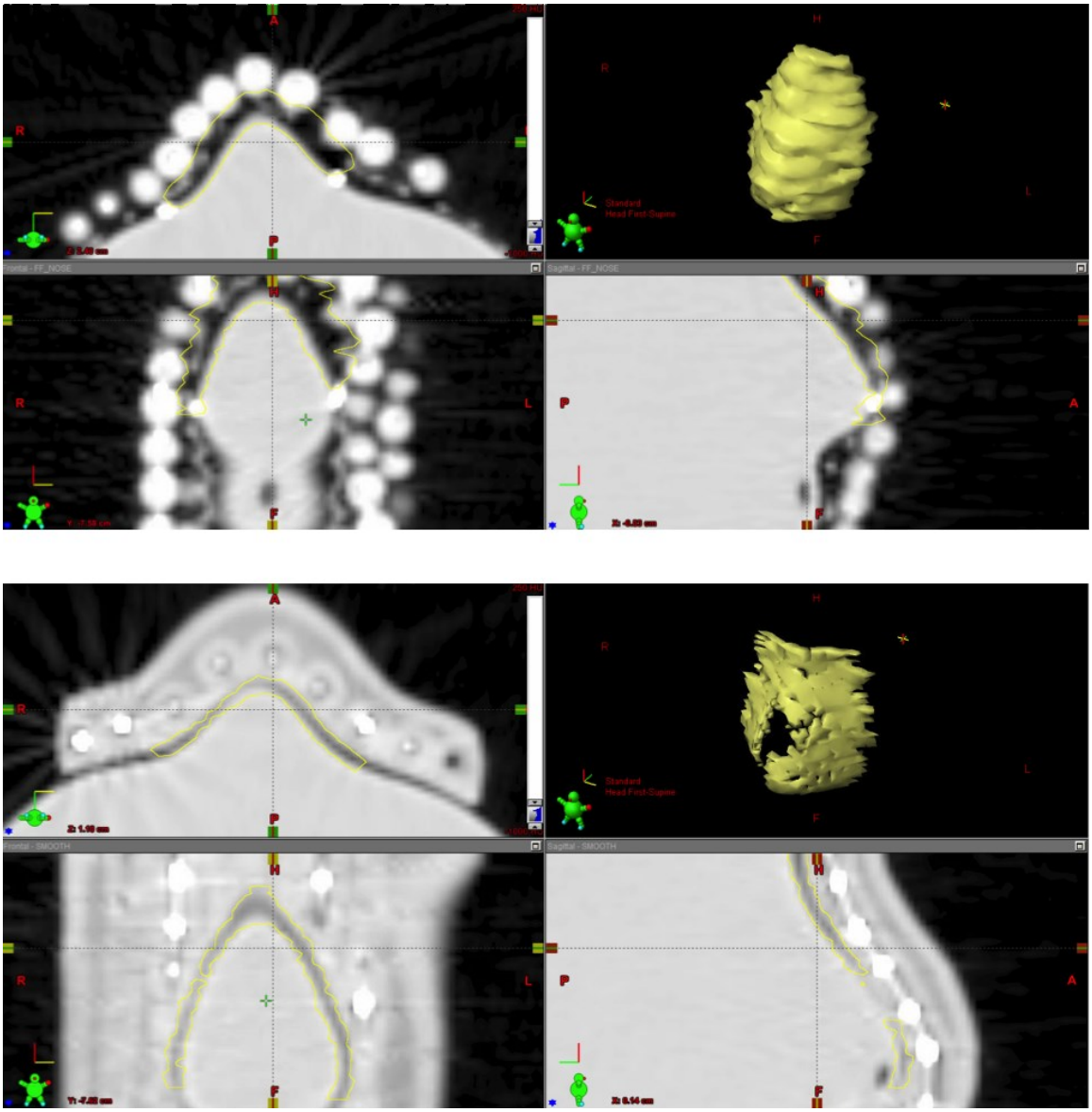

Figure 43: Contoured air gaps generated in Eclipse for nose experiment. Top: Freiburg flap. Bottom: 3D printed applicator.

Table 7: Air gap volumes contoured in Eclipse for 3D printed and Freiburg flap applicators.

Airgap		
	3D (cm^3)	Flap (cm^3)
Foot	0.65	31.8
Nose	7.18	17.08

The 3D printed applicators proved to minimize the air gaps between the catheter and the treatment plane. Although that did not have a significant impact on the experiment involving the treatment site on the foot in this study, it does give the medical physicist more control over the plan. The distance from source to skin is known to a much better accuracy with the 3D printed applicator. The silicone spheres making up the flap material have a diameter of 5 mm, but when they are sewn onto the mask, assuming the mask conforms to the body very precisely, an added distance of 5 mm is added. This could result in the over irradiation of normal tissue extending beyond the tumour. Referring to Figure 29, a large distance between source and treatment plane results in a dose distribution coming from the shallow sloped, linear portion of the inverse square curve, meaning there will not be a large dose gradient from CTV to normal tissue.

Looking at the air gaps generated in the 3D applicator for both the foot and the nose study, there is great disparity in the volumes. This is due primarily to the smoothing feature in the applicator creation process. When the CT data is taken, there are discrete layers making up the structure's resolution. When the object is smoothed, a lot of that information is lost. The result is an applicator that may not fit as well as it would have it retained all of its resolution. This result is amplified in highly irregular surfaces, like the nose, resulting in a small volume of air between the applicator and the surface. Regardless of whether or not one chooses to smooth, the air gap generated by the 3D printed applicator is much smaller than the gap created by the Freiburg flap.

3.4 Clinical Cases

3.4.1 Patient with Basal Cell Carcinoma

In order to assess the efficacy of the 3D printed applicator technique it needed to be incorporated into a clinical case to be used on a patient receiving radiation therapy. A patient diagnosed with a basal cell carcinoma on his nose was chosen as the first candidate, providing a highly irregular surface for which to construct an applicator. In order to give the patient more comfort during treatment, any sharp pieces on the applicator were smoothed after printing with a propane torch plus knife adaptor (Weller P2K Portasol). Care was taken to maintain the applicator's unique, form fitting shape. When the patient came in for a second CT scan, the fit of the applicator was assessed for both proximity to the skin and comfort. The applicator fit very well to the contours of the patient's nose, as can be seen in Figure 33B. Once the patient was scanned, the CTV was contoured by a radiation oncologist for treatment planning.

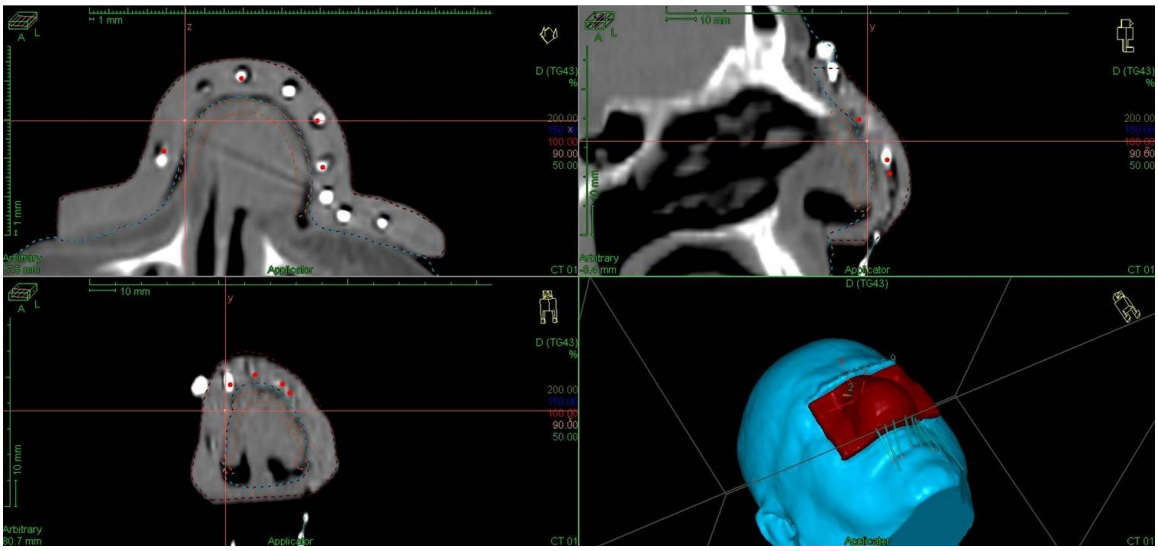

Figure 44 - Oncentra view of CTV for BCC patient. Red dotted line represents CTV while blue dotted line is the patient's body.

The radiation plan for the patient was created by a medical physicist with a prescription dose of 55 Gy, in 20 fractions. Both eyes were contoured as OARs to assess normal tissue sparing. It was found that due to the proximity of the treatment area to the left eye, a sufficient dose distribution to the tumour could not be achieved while sparing the eye. Referring to Table 8, the maximum dose to the left eye was 240 cGy (87% the value of the prescription dose). The dose limit for the lens of the eye to develop cataracts is 200 cGy, with decreasing latent period with increasing dose (10). The highly customizable nature of 3D printed applicators offered a potential solution. Inserting sheets of lead over the eye as a shielding mechanism could lower the dose to an acceptable level. In this case, where the original dose to the eye was close to the prescription dose, it would require many half-value layers of lead (HVL_{Pb} = 4.8 mm) in order to reduce the dose to a level that would be acceptable.

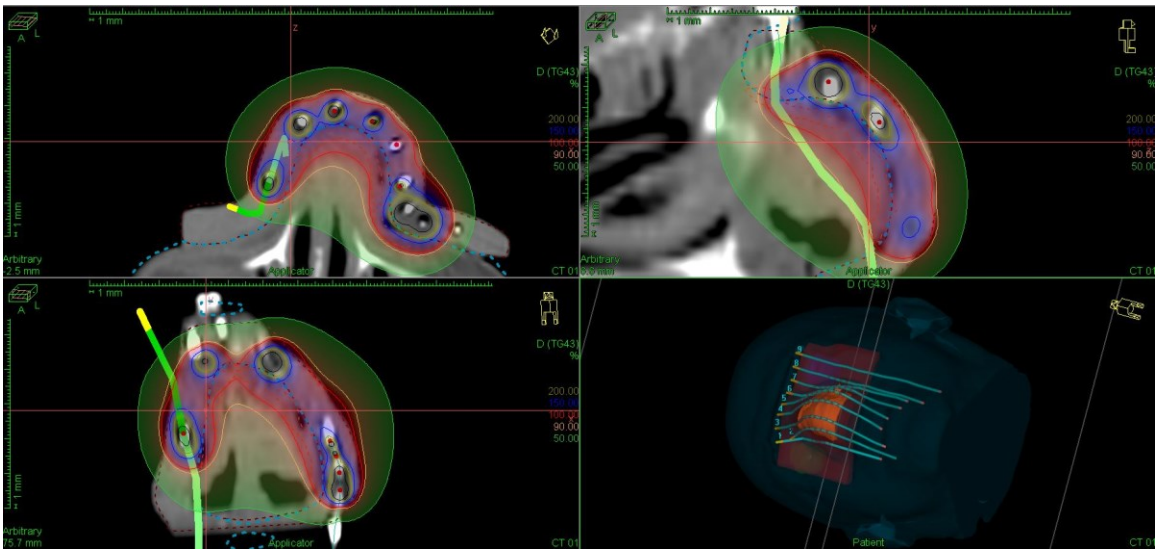

Figure 45 - Dose distribution generated for a patient with basal cell carcinoma of the nose. Red lines denote 100% isodose and the green tube represents the reconstructed catheter for potential dwell positions.

Table 8 - Dosimetric properties for the BCC patient.

Name	Minimum dose (cGy)	Maximum dose (cGy)	Mean dose (cGy)
CTV	159	565	285
RT Eye	23	58	35
LT Eye	35	240	74

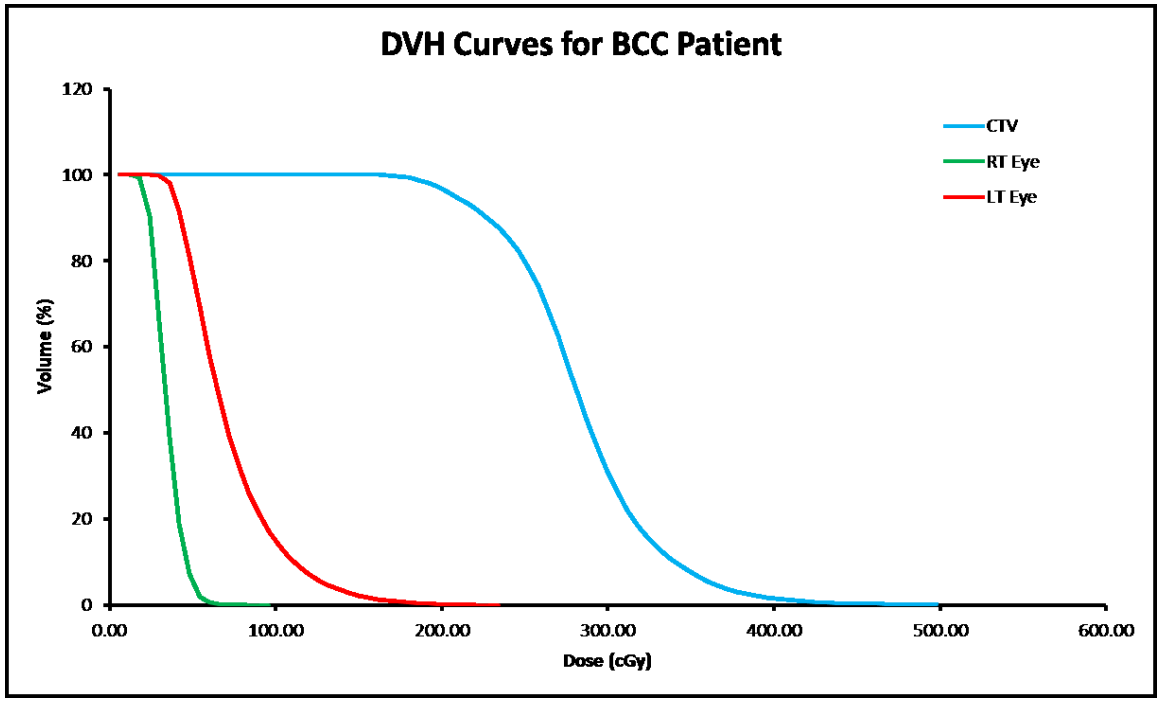

Figure 46 - DVH curves for the BCC patient. Plot shows CTV coverage (blue), right eye toxicity (green), and left eye toxicity (red).

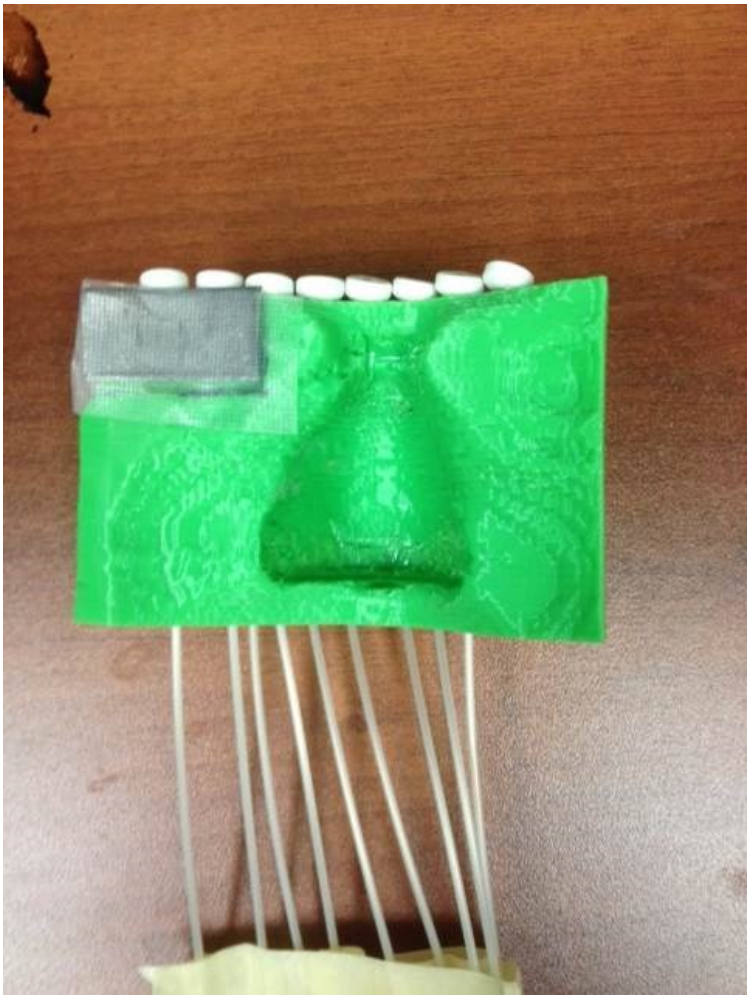

Figure 47 - 3D printed nose applicator for BCC patient emphasizing the lead shielding over the left eye. A slot was created to allow the lead to be inserted while maintaining a flush fit to the surface of the patient.

3.4.2 Patient with Rhabdomyosarcoma

With the applicator designed for the patient with rhabdomyosarcoma of the soft palate, it was desired that a compartment be constructed to insert lead shielding to lower the dose being delivered to the base of the tongue. As this was done as more of a precautionary step, a slot of roughly 50% of the value of a half-value layer of lead was added. Despite the applicator being sufficient to treat the patient, it was not used on the grounds that there were not explicit guidelines for sterilization. Since the applicator would be going into the body each day, with the potential for open sores to develop

during radiation treatment, the risk of infection resulted in the use of a different type of applicator material, fabricated by the patient's dentist, which allows daily cleaning procedures that have been clinically reviewed and accepted. Nevertheless, Figure 47 shows a Blender rendered image of the applicator designed for this patient, complete with catheter tunnels, air hole, and a 2.2 mm slot for lead shielding.

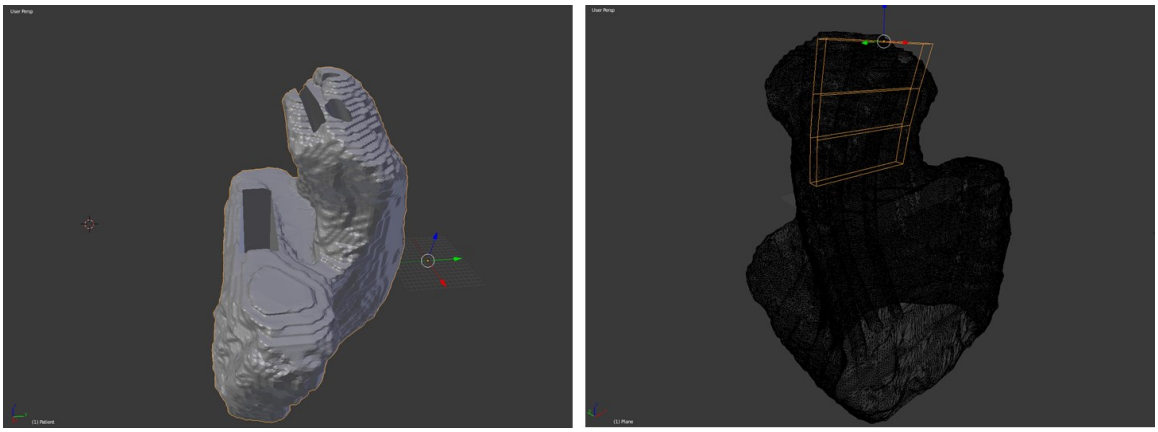

Figure 48 - Blender image of a mouth applicator fabricated for a patient with rhabdomyosarcoma of the soft palate. Left: Outer view. Right: Wireframe view, orange box showing the location of the shielding slot.

3.5 Other benefits of using 3D Printed Applicators

One of the main advantages of using 3D printed brachytherapy applicators as opposed to Freiburg flaps or wax moulds is that there is very little human intervention. The laborious and manual process of sewing the flaps onto the mask, or heating individual wax sheets to create a mould can create great disparity between therapists resulting in no two flap plans or wax plans being the same. On the other hand, using a 3D printed applicator once an applicator is designed programmatically, each time it is printed yields the same result. As of today, the only apparent downside in using 3D printed applicators lies in the duration of print time. Currently, a company based in San Francisco (Autodesk) is developing 3D printing software capable of printing at speeds of 24 times

faster than current printers. Project Esher, a new technology combining hardware and software, focuses on pushing material out of the nozzle, opposed to being drawn in by a gear system (29). The printer itself is larger and incorporates multiple extruder to work together to print an object. Depending on the size of the applicator, the time it takes to print could be anywhere between 3 and 30 hours. This number can vary greatly depending on parameters such as infill percent and print speed. In order to give each print the highest probability of success, the print speed for all the applicators made using Ninjaflex filament was kept at its lowest setting of 18 mm/s. As a result, the average applicator typically takes between 8-10 hours, allowing it to be started at the end of the day and be finished at the beginning of the next day, as it requires no supervision. The print time is something that will likely see a drastic decrease as the technology of 3D printers improves.

CHAPTER 4 CONCLUSION

In this study, we investigated the feasibility of using 3D printed surface applicator for the administration of HDR brachytherapy for superficial lesions. Most skin cancers respond very well to radiation as a primary treatment method and incorporating 3D printed applicators could lead to more patients being successfully treated. It was our hypothesis that 3D printed applicators would offer comparable dose distributions, reproducibility, conformity with the patient leading to smaller air gaps between applicator and treatment site, and decrease the labourious nature of applicator fabrication. In order to move from an idea to a fully fledged treatment modality, many steps need to be taken to ensure efficacy and patient safety, among other things. Preliminary studies show that 3D printed applicators offer better patient conformity, reduced air gap, and convenience to both patient and therapist when administering HDR brachytherapy radiation. The treatment plans created for 3D printed applicators showed that they offer plans equivalent to or better than their Freiburg Flap counterparts. The current practice involves a great deal of therapist time to manufacture the applicator and the advancement of 3D printing technology has taken the human aspect out of the process. Once the catheter construction is automated in Blender, the only time consuming component of the process will be the printing of the applicator itself, which does not involve user intervention and is likely to decrease as 3D printing technology advances. Although the plans created with the 3D applicator show better dose distributions for irregular surfaces when compared to FF plans, the results shown here are for constant catheter distances to the treatment plane. The next step in this research is to optimize the catheter placement within the applicator itself. Assigning each tunnel its own variable distance, a dose distribution that follows the

contours of the CTV could be generated while sparing the surrounding tissue. Although there were two clinical cases outlined in this research, it is important that this method be tested on many more. 3D printed applicators could be incorporated into the clinic to treat patients with tumours that are large or small, regular or irregular, or even within cavities of the body. 3D printed applicators address deficiencies of Freiburg Flaps requiring less time and labour, better conformity for highly irregular surfaces, eliminating the need for a mask, providing lower volume of air gaps, and an overall more convenient approach for the patient. 3D printing technology has been proven to have many applications to radiation therapy including MERT, chest wall bolus, gynecological brachytherapy applicators, and now superficial brachytherapy applicator for the treatment of skin cancer.

BIBLIOGRAPHY

1. Proksch E, Brandner JM, Jensen J-M. The skin: an indispensable barrier. Exp Dermatol. 2008 Dec;17(12):1063–72.

2. American Cancer Society. Skin Cancer Facts [Internet]. [cited 2015 Apr 13]. Available from: http://www.cancer.org/cancer/cancercauses/sunanduvexposure/skin-cancer-facts

3. WHO. Skin Cancers [Internet]. World Health Organization; Available from: http://www.who.int/uv/faq/skincancer/en/index1.html

4. Cancer Facts and Figures 2016 [Internet]. American Cancer Society; [cited 2016 Mar 17]. Available from: http://www.cancer.org/acs/groups/content/@research/documents/document/acspc-047079.pdf

5. Boundless. Structure of the Skin: Epidermis [Internet]. Boundless Anatomy and Physiology; 2016. Available from: https://www.boundless.com/physiology/textbooks/boundless-anatomy-and-physiology-textbook/integumentary-system-5/the-skin-64/structure-of-the-skin-epidermis-394-7794/

6. Mayo Clinic. Squamous Cell Carcinoma of the Skin [Internet]. Mayo Clinic; 2016. Available from: http://www.mayoclinic.org/diseases-conditions/squamous-cell-carcinoma/home/ovc-20204362

7. NIH. Melanoma of the Skin [Internet]. National Cancer Institute; Available from: http://seer.cancer.gov/statfacts/html/melan.html

8. Skin Cancer Treatment Options [Internet]. Skin Cancer Foundation; Available from: http://www.skincancer.org/skin-cancer-information/squamous-cell-carcinoma/scc-treatment-options

9. Delaney G, Jacob S, Featherstone C, Barton M. The Role of Radiotherapy in Cancer Treatment: Estamating Optimal Utilization from a Review of Evidence Based Clinical Guidelines. Cancer. :1129–37.

10. Hall E, Giaccia A. Radiobiology for the Radiologist. 7th ed. Lippincott Williams & Wilkins; 2012.

11. Attix F. Introduction to Radiological Physics and Radiation Dosimetry. John Wiley & Sons, Inc.; 2004.

12. Khan F. The Physics of Radiation Therapy. Fourth. Lippincott Williams & Wilkins; 2010.

13. Almond P. Clinical Applications of the Electron Beam. John Wiley & Sons, Inc.; 1976.

14. Kharofa J, Currey A, Wilson JF. Patient-Reported Outcomes in Patients With Nonmelanomatous Skin Cancers of the Face Treated With Orthovoltage Radiation Therapy: A Cross-Sectional Survey. Int J Radiat Oncol. 2013 Nov;87(4):636–7.

15. Strnad V, Potter R, Kovacs G. Practical Handbook of Brachytherapy. International Medical Publishers; 2014.

16. Peinemann F, Grouven U, Hemkens LG, Bartel C, Borchers H, Pinkawa M, et al. Low-dose rate brachytherapy for men with localized prostate cancer. In: The Cochrane Collaboration, editor. Cochrane Database of Systematic Reviews [Internet]. Chichester, UK: John Wiley & Sons, Ltd; 2011 [cited 2016 Jul 13]. Available from: http://doi.wiley.com/10.1002/14651858.CD008871.pub2

17. Meigooni AS. Dosimetry of interstitial brachytherapy sources: recommendations. Med Phys. 1995;22(2):2.

18. Devlin P. Brachytherapy - Applications and Techniques. Lippincott Williams & Wilkins; 2007.

19. Goyal U, Kim Y, Tiwari HA, Witte R, Stea B. A pilot study of ultrasound-guided electronic brachytherapy for skin cancer. J Contemp Brachytherapy. 2015;5:374–80.

20. Ghebremichael BT. Dosimetric Comparison of Inverse Planning by Simulated Annealing (IPSA) and Dose Points Optimized Treatment Plans in High Dose Rate (HDR) Brachytherapy of Skin Lesions Using Freiburg Flap Applicator [Internet]. Florida Atlantic University Boca Raton, Florida; 2014 [cited 2016 Jul 13]. Available from: http://fau.digital.flvc.org/islandora/object/fau%3A30774/datastream/OBJ/download/Dosimetric_comparison_of_inverse_planning_by_simulated_annealing__IPSA__and_dosepoints_optimized_treatment_plans_in_high_dose_rate__HDR__brachytherapy_of_skin_lesions_using_Freiburg_flap_applicator.pdf

21. Sarudis S. Dose distribution beneath the Leipzig skin applicator set. Print Stockh Thesis Univ Stockh [Internet]. 2006 [cited 2016 Jul 13]; Available from: http://ki.se/sites/default/files/sebastian_sarudis_exjobb.pdf

22. D'Amours M, Pouliot J, Dagnault A, Verhaegen F, Beaulieu L. Patient-Specific Monte Carlo-Based Dose-Kernel Approach for Inverse Planning in Afterloading Brachytherapy. Int J Radiat Oncol. 2011 Dec;81(5):1582–9.

23. Su S. Design and production of 3D printed bolus for electron radiation therapy. 2014 [cited 2016 Jun 29]; Available from: https://dalspace.library.dal.ca/handle/10222/54027

24. Cunha JA, Mellis K, Sethi R, Siauw T, Sudhyadhom A, Garg A, et al. Evaluation of PC-ISO for Customized, 3D Printed, Gynecologic 192-IR HDR Brachytherapy Applicators. J Appl Clin Med Phys. 2015;16(1):246–53.

25. Robar J. 3D Printed Bolus for Chestwall Radiation Therapy. Poster presented at: Estro35; 2016; Turin.

26. Schumacher MW, Lasso A, Chandra J, Falkson CB, Schreiner LJS, Fichtinger G. 3D printed surface mould applicator for high-dose-rate brachytherapy. In: SPIE Medical Imaging [Internet]. International Society for Optics and Photonics; 2015 [cited 2016 Apr 14]. p. 94152E–94152E. Available from: http://proceedings.spiedigitallibrary.org/proceeding.aspx?articleid=2210352

27. NinjaTek. NINJAFLEX® [Internet]. Available from: http://ninjatek.com/products/ninjaflex-filaments/

28. Fulkerson RK, Micka JA, DeWerd LA. Dosimetric characterization and output verification for conical brachytherapy surface applicators. Part II. High dose rate 192Ir sources. Med Phys. 2014 Feb;41(2):22104.

29. New Advancements in 3D Printing to Improve Speed and Scale [Internet]. Autodesk, Inc; 2016. Available from: https://spark.autodesk.com/blog/new-advancements-3d-printing-improve-speed-and-scale